AIAA Aviation
22-26 June 2015, Dallas, TX
22nd AIAA Computational Fluid Dynamics Conference

Unstructured Grid Simulations of Transonic Shockwave-Boundary Layer Interaction-Induced Oscillations

Keerti K. Bhamidipati*
Air Force Test Center – Edwards AFB, California 93524, U.S.A.
Daniel A. Reasor Jr.† and Crystal L. Pasiliao‡
Air Force Research Laboratory – Eglin AFB, Florida 32542, U.S.A.

Shockwave oscillations at transonic freestream conditions on airfoil and wing models were simulated using unstructured computational fluid dynamics techniques. The models utilized either the OAT15A or NACA 64A204 airfoil profile. The node-based finite-volume solver developed by NASA's Langley Research Center, FUN3D version 12.4, was employed. Mixed element type grids were constructed using the AFLR libraries integrated into the CREATE™-MG Capstone mesh generation software. The grids contained triangle elements on the airfoil/wing surface, prismatic elements in the boundary layer, and tetrahedral elements in the fluid domain. The work presented herein demonstrates that while unstructured grid URANS simulations are capable of predicting shockwave oscillations, frequency and damping of the oscillations are sensitive to numerous grid characteristics. Furthermore, results show that the inclusion of non-airfoil geometries in models does not significantly alter the primary shockwave oscilaltion frequency.

Nomenclature

α	=	angle of attack, deg.
c	=	chord length, in.
C_d	=	coefficient of drag
$C_{f,x}$	=	streamwise skin friction coefficient
C_l	=	coefficient of lift
C_p	=	coefficient of pressure
f	=	frequency
L^*_{ref}	=	reference physical length, in.
r	=	grid refinement factor
Δs	=	surface element resolution, in.
U^*_{ref}	=	reference physical velocity, in./sec.
x/c	=	non-dimensional chord-wise location
ζ	=	damping

I. Introduction

Air vehicles operating in transonic, supersonic, and hypersonic regimes can experience shockwave oscillations resulting from shockwave-boundary layer interaction (SBLI).[1] These shockwave oscillations can affect the lift and moments experienced by the air vehicle in localized areas or over large regions. However, even with modern computational fluid dynamics (CFD) tools, it is difficult to predict SBLIs. Oscillations that occur in the transonic regime are of particular interest to the authors because of research that suggests that transonic limit-cycle oscillation (LCO) phenomenon observed on elastic wings may be related to self-sustained shock-buffet.[2] Dedicated wind tunnel testing has been conducted to provide a better understanding of the

*Aerospace Engineer, Testing Techniques Flight, 812th Test Support Squadron, AIAA Member
†Aerospace Engineer, Munition Aerodynamic Sciences Branch, Senior AIAA Member
‡Technical Advisor, Munition Aerodynamic Sciences Branch, Senior AIAA Member

conditions at which these shockwave oscillations occur, and allow researchers to improve their predictive tools.[3–5] All transonic shockwave oscillation computational research efforts to date have utilized structured-grid CFD solvers and, therefore, structured grids.[6–12] While structured-grid CFD solvers lend themselves to higher-orders of spatial and temporal accuracy, compatible grids are difficult to generate on complex aircraft and missile geometries.[13] Being able to utilize an unstructured CFD solver to predict transonic shock-buffet would enable researchers to study the effect of shockwave oscillations on the aerodynamics of real-world air vehicle designs.

I.A. Background

At transonic Mach numbers, buffeting can cause large-scale lift oscillations that can limit an aircraft's flight envelope.[8] These large-scale lift oscillations are caused by a separation of the viscous boundary layer on the upper surface of the wing either at the trailing edge or at the foot of the shockwave. Once a sufficiently high angle of attack (α) is reached, the separation region extends from the foot of the shock to the trailing edge of the airfoil. Once this separation region is formed, the flow becomes very unsteady and the shockwave position oscillates a significant distance of the wing chord. Separation is a strictly viscous phenomenon that must be modeled by an approach that solves the compressible Navier–Stokes equations with appropriate boundary conditions.

Scaling arguments[14] and known discrepancies between computational predictions of LCO amplitudes based on inviscid computations[15,16] reveal that a Navier–Stokes model is needed to accurately capture separated flow effects due to SBLI or due to large wing tip angle of attack. Simulations have shown that Reynolds-averaged Navier–Stokes (RANS) equations predict significantly different shock locations compared to Euler, and that the Spalart–Allmaras (SA) turbulence model is capable of predicting large shockwave movement on airfoils.[17]

Crouch et al.[8] examined the use of global-stability criterion to predict this shock buffet onset. Their findings indicate that while numerical dissipation is necessary for shock capturing, it can contaminate the solution near the stability boundary, and that the boundary can be dependent on the turbulence model employed. The unsteady RANS (URANS) simulations using the structured grid solver OVERFLOW2,[9] indicate that the amplitude of lift coefficient of a two-dimensional (2-D) airfoil exposed to self-sustained shock oscillations is a function of turbulence model (e.g., SA, k-ω, SST), computational flux functions (e.g., Liou AUSM+ Flux Split, Roe, HLEE++), and flux limiter (e.g., none, Koren, Minmod, VanAlbada). They also observed that the sustained oscillations observed in one version of OVERFLOW2 (2.1ae) were not reproducible using an updated version (version 2.1o).

Recent wind tunnel experiments[18] have demonstrated that shockwaves are influenced by external noise sources or that a feedback loop between the shock position and the noise generated at the wing trailing edge can be a dominant buffet mechanism. This observation emphasizes the importance of sufficiently resolving pressure waves at the trailing edge of airfoils and wings any may indicate the need for highly-resolved, low-dissipation aeroacoustic simulations.

I.B. Validation Dataset

Experimental data from OAT15A airfoil tests performed in the French aerospace research center (ONERA) S3Ch wind tunnel was used as a validation dataset to better understand the modeling and simulation (M&S) requirements for predicting transonic shockwave oscillations. The OAT15A is a supercritical airfoil designed to operate at transonic speeds. S3Ch experiments were conducted on a 9 inch chord (c) length , 3 c span width test article instrumented with numerous static pressure orifices and Kulite® pressure transducers on the upper and lower surfaces. The test article experienced sustained shockwave oscillations on the upper surface at a frequency of approximately 70 Hz, at Mach 0.73, Reynolds number 3×10^6 freestream conditions. Most notably, the shockwave oscillations observed on the OAT15A are more comparable in nature to those predicted on the NACA 64A204 than those observed on the NACA 0012,[3] due to the larger shockwave travel distances and lower shockwave oscillation frequencies experienced by the higher speed OAT15A and NACA 64A204 airfoils.

The ONERA OAT15A experiments provide a useful dataset because Mach number and airfoil α were precisely varied to characterize oscillation onset conditions and the periodic motion of the shockwave on the airfoil upper surface. Experimental airfoil surface pressure data was also gathered at a lower α where shockwave oscillations were not present, to facilitate the verification and validation (V&V) of CFD methods

at an easier to simulate steady flowfield condition. The details of the S3Ch experiments conducted by ONERA, and summarized by Jacquin et al.[5] and Deck[6] were utilized. The OAT15A geometry and selected experimental data from wind tunnel testing were retrieved from the Advanced Turbulence Simulation for Aerodynamic Application Challenges (ATAAC) website.[19]

The α=2.5° and 3.5° conditions were of particular interest for the validation work performed. In the S3Ch experiments, no shockwave buffet was observed on the airfoil at α=2.5°. At the α=3.5° condition, the buffet was fully established, and shockwave travel distance of 20% of the airfoil chord length was noted. Oil flow visualization showed the separation line due to the shockwave to be parallel to the airfoil leading edge over most of the airfoil span. Three dimensional effects were reported only near the side walls, and affected approximately 10% of the test article span at both wall boundaries.[5]

I.C. Build-up to F-16 Simulations

An area of interest for the researchers is the ability to predict and characterize aerodynamic properties of the LCO phenomenon observed on an F-16 aircraft with stores,[20] which has been demonstrated to be highly sensitive to small aerodynamic changes.[21] Simulating transonic shockwave oscillations on the F-16 wing airfoil (NACA 64A204) using knowledge gained from OAT15A validation simulations, was seen as the next logical step to towards understanding how the shock-buffet contributes to LCO behavior observed on F-16 wings. The NACA 64A204 airfoil simulated was chosen to represent the butt-line 159 (BL159) location of the F-16 wing, and therefore has a chord length of 62 inches. The flowfield at the BL159 location is of interest due to its proximity to the underwing missile pylon located at BL157,[22] and the ability to compare results to previous LCO-configuration F-16 wing CFD research.[22–24]

II. Simulation Setup

II.A. CFD Solver Details

The unstructured CFD code utilized was NASA Langley Research Center's FUN3D v12.4.[25] FUN3D is a node-based finite-volume solver that is being actively developed. Simulations were performed using the non-dimensional Navier–Stokes stokes equations, and treating the air as a compressible, calorically perfect gas. The majority of simulations used the one-equation "standard" Spalart–Allmaras (SA) turbulence model.[26] A few simulations were preformed using the Menter SST two-equation turbulence model with strain source term,[27] in order to contrast results from two of the most commonly used turbulence models. A second-order accurate spatial scheme, optimized second-order accurate backward differencing temporal scheme, and Roe's flux without a flux limiter were utilized for all simulations.

Most steady RANS (SRANS) simulations were run for 5000 iterations at a constant CFL number of 200, and constant turbulence CFL number of 50 regardless of turbulence model utilized. Only steady SST simulations of NACA 64A204 airfoils employed a ramping of CFL from 1 to 200, and turbulence CFL from 1 to 50, over the first 50 iterations to prevent the simulation failing due to the large pressure differences at the trailing edge. Unsteady RANS (URANS) simulations were run using a non-dimensional time step equivalent to 100 steps per advective time scale, allowing for up to 30 subiterations, with a constant CFL number of 50 and constant turbulence CFL number of 30. The advective time scale is defined as physical length of the airfoil divided by the reference velocity (L^*_{ref}/U^*_{ref}). For the OAT15A airfoil the non-dimensional time step used (0.1233) corresponds to a dimensional time step of 9.51×10^{-6} seconds. For the NACA 64A204 airfoil the non-dimensional time step used (0.826) corresponds to a dimensional time step of 6.28×10^{-5} seconds. For almost all of the cases simulated, the maximum 30 subiterations were executed at each time step because simulations with moving shocks did not show an order of magnitude improvement in subiteration residuals. The time step of 1000 steps per advective scale was tested using some grids but demonstrated minimal change in number of subiterations executed or predicted lift force.

II.B. Grid Construction

All simulations presented herein utilized mixed element type viscous grids. These grids are also commonly referred to as hybrid element grids or hybrid grids. The grids contained triangle elements on the airfoil/wing surface, prism elements in the boundary layer region, and tetrahedral elements elsewhere.

The OAT15A airfoil grids constructed to validate the M&S tools progressed from the small one-spanwise-element width meshes up to very large $3\,c$ span width meshes that represented the full span S3Ch wind tunnel test article. To enable comparisons between grids of different widths, and simulate ideal airfoil behavior, symmetry wall boundaries were prescribed at both ends of the airfoil span. One-element wide meshes were constructed to simulate ideal 2-D airfoil behavior using a three-dimensional (3-D) CFD solver. Wider meshes of $1/12\,c$, $1/4\,c$, and $3\,c$ span width airfoils were used to study the feasibility of simulating shockwave oscillations on 3-D wings. The $3\,c$ span airfoil and wing OAT15A grids grids were built using elements size settings that demonstrated the best results during $1/4\,c$ span grid simulations. Non-airfoil models constructed consisted of a one-element width airfoil with 2-D store, and an OAT15A wing with wing-tip geometry roughly representative of the F-16 tip launcher. All OAT15A grids utilized 35 cells to model the viscous boundary layer up to 0.177 inches thick, with a first layer height of 6.0×10^{-5} inches and a cell height grow rate of 1.2. The fluid domain element global size increment allowed was 1.1. For airfoil grids, the computational domain was represented by a cylinder with the planar surfaces coincident with the ends of the airfoil span. For wing grids, the computational domain was represented by a half-sphere with the planar surface coincident with the wing root. The non-planar farfield extents were located at a distance of $50\,c$ away. The grids constructed based on the OAT15A airfoil grids are presented in Tables 1, 2, and 3.

Initial OAT15A simulations utilized meshes with a very fine airfoil discretization. A surface element size of 0.02 inches (1/450 of the 9 inch airfoil chord length) was specified in order to provide at least 400 mesh nodes on the upper and lower airfoil surfaces. The very fine discretization was expected to better resolve the predicted shock location. However, the 0.02 inch surface element size quickly becomes too computationally expensive for simulating 3-D geometries. In order to study effect of decreasing airfoil surface mesh resolution, the prescribed surface element size was doubled to 0.04, then again to 0.08, and finally to 0.16 inches. These surface discretizations are referred to as fine, medium, and coarse meshes, respectively. A smaller surface element size of 0.01 inch on the trailing edge (TE) was tested on the $1/4\,c$ span medium airfoil mesh to study the effect of increased aft-region mesh detail on CFD simulation predictions. The TE refinement resulted in 5 mesh nodes across the height of the airfoil trailing edge. Properties of $3\,c$ span width models with and without trailing edge refinement are presented in Table 3 to enable comparison of mesh size growth due to TE mesh refinement versus increased surface mesh resolution.

NACA 64A204 airfoil grids were generated based on the geometry and surface discretization that demonstrated the best results for OAT15A airfoil grid simulations. The $1/4\,c$ span width NACA 64A204 airfoil geometry also allowed for finer surface discretization meshes that were not prohibitively large to generate and simulate. Details of NACA 64A204 airfoil grids are presented in Table 4. Surface element sizes of 0.25 and 0.5 inches are described as medium and fine respectively. The medium surface resolution contains at least 100 mesh nodes on the upper and lower airfoil surfaces. The fine resolution doubles the number of nodes on the surface. Trailing edge element size was set to 0.02 inch to provide aft region refinement, and resulted in 5 grid points across the height of the TE. All NACA 64A204 grids utilized 46 cells to model the viscous boundary layer up to 0.878 inches thick, with a first layer height of 4.0×10^{-5} inches and a cell height grow rate of 1.2. Grids with fluid domain element global size increments of 1.1, 1.02, and 1.05 were used to study the effect to slower volume element size growth.

Grid refinement factor, r, was calculated for grids that shared common geometry using the equation:[28]

$$r = (N_1/N_2)^{1/d}, \tag{1}$$

where N_1 and N_2 are the number of cells or nodes in the finer and coarser grids being compared, and d is the spatial dimension (3 in this work). Since FUN3D is a node-centered solver, the number of grids points are used in the refinement factor calculations provided in Tables 2, 3, and 4.

Two significant changes exist between the grids utilized in the current work, and airfoil grids utilized by the researchers in their previous shockwave oscillation work.[17] The AFLR surface and volume meshers integrated into the CREATE$^{\text{TM}}$-MG Capstone version 4.0.3 mesh generation software enabled both of these changes. First, all OAT15A grids are built for full wall integration (with a first wall-normal grid spacing corresponding to a $y^+ < 1$) because FUN3D does not utilize wall-functions for viscous simulations. Second, previous NACA 64A204 airfoil grids had uniform spanwise element spacing, due to limitations with the ICEM CFD$^{\text{TM}}$mesh generation software which required narrow span airfoil models to be built as 2-D grids and then extruded in the spanwise direction. This extrusion method is identical to the technique utilized by Deck[6] for generating the structured 2-D/3-D OAT15A grids. An extruded OAT15A airfoil mesh is contrasted against a 3-D airfoil mesh with non-uniform spanwise spacing in Figure 1. Although full wall integration meshes

Table 1. OAT15A airfoil-based very fine (VF) surface resolution ($\Delta s = 0.02$ in.=1/450 c) grids constructed.

Abbreviated Name	Span	Grid Points ($\times 10^6$)	Elements ($\times 10^6$)
1elem$W$-VF-airfoil	0.02 in. (1 element)	0.100	0.196
1elem$W$-VF-airfoil-w2Dstore	0.02 in. (1 element)	0.228	0.469
1/12 cW-VF-airfoil	0.75 in. (1/12 c)	1.50	4.18
1/4 cW-VF-airfoil	2.25 in. (1/4 c)	4.82	12.2

Table 2. 1/4 c **width (2.25 in.) span OAT15A airfoil grids constructed.**

Abbreviated Name	Surface Resolution (Δs)	Grid Points ($\times 10^6$)	Elements ($\times 10^6$)	r
1/4 cW-M-airfoil	0.08 in. (1/112.5 c)	0.334	0.835	-
1/4 cW-F-airfoil	0.04 in. (1/225 c)	1.32	3.41	1.58
1/4 cW-VF-airfoil	0.02 in. 1/450 c)	4.82	12.2	1.54
1/4 cW-C-airfoil-wTEref	0.16 in. (1/56.25 c)	0.378	0.937	-
1/4 cW-M-airfoil-wTEref	0.08 in. (1/112.5 c)	0.574	1.48	1.15; 1.20†
1/4 cW-F-airfoil-wTEref	0.04 in. (1/225 c)	1.39	3.67	1.34; 1.02†

† r computed using N_2 as grid with same Δs but without trailing edge refinement
In abbreviated grid names: C = coarse surface mesh resolution; M = medium surface mesh resolution; F = fine surface mesh resolution; VF = very fine surface mesh resolution; TEref = trailing edge cell refinement, resulting in 5 grid points along height of trailing edge

Table 3. 3 c **width (27 in.) span OAT15A airfoil-based grids constructed.**

Abbreviated Name	Surface Resolution (Δs)	Grid Points ($\times 10^6$)	Elements ($\times 10^6$)	r
3 cW-M-airfoil	0.08 in. (1/112.5 c)	3.73	9.19	-
3 cW-M-airfoil-wTEref	0.08 in. (1/112.5 c)	6.46	16.2	1.20
3 cW-F-airfoil	0.04 in. (1/225 c)	13.7	33.9	1.54*
3 cW-M-wing-wTEref	0.08 in. (1/112.5 c)	6.46	16.4	-
3 cW-M-wing-wTEref-wTipL	0.08 in. (1/112.5 c)	8.26	20.8	-

* r computed using N_2 as 3cW-M-airfoil grid
In abbreviated grid names: M = medium surface mesh resolution; F = fine surface mesh resolution; TEref = trailing edge cell refinement, resulting in 5 grid points along height of trailing edge; wTipL = with wing-tip geometry representative of tip launcher

Table 4. 1/4 c **width (15.5 in.) span NACA 64A204 airfoil grids constructed and global size increment (GSI) specified.**

Abbreviated Name	GSI	Surface Resolution (Δs)	Grid Points ($\times 10^6$)	Elements ($\times 10^6$)	r
1/4 cW-M-airfoil-wTEref	1.1	0.50 in. (1/124 c)	2.00	5.06	-
1/4 cW-F-airfoil-wTEref	1.1	0.25 in. (1/248 c)	3.25	8.17	1.18
1/4 cW-F-airfoil-wTEref-gsi1.05	1.05	0.25 in. (1/248 c)	4.21	11.1	1.09
1/4 cW-F-airfoil-wTEref-gsi1.02	1.02	0.25 in. (1/248 c)	9.59	30.8	1.32

contain an increased number of boundary layer elements compared to wall function meshes, Capstone meshes were 25-75% smaller than ICEM CFD^{TM}meshes for the equivalent surface element sizes. This was due to the ability of AFLR generated 3-D fluid domain elements to transition from very fine prismatic elements matched to the surface discretization, to larger 3-D tetrahedral elements as distance from the airfoil surface increased. Additionally, the ability to adjust mesh parameters systematically and generate meshes of varying element sizes in a repeatable manner was greatly improved with Capstone compared to ICEM CFD^{TM}.

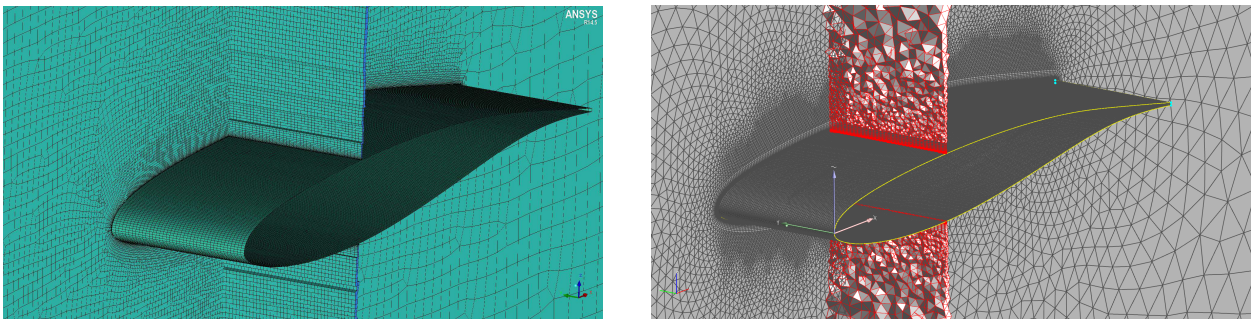

(a) ICEM CFD^{TM}mesh (b) Capstone AFLR mesh

Figure 1. Comparison of an airfoil mesh with uniform spanwise element spacing (constructed with ICEM CFD^{TM}), and against a mesh with non-uniform spanwise volume elements transitioning from very fine prismatic elements in the boundary layer to larger tetrahedral elements away from the airfoil surface (constructed with CREATE^{TM}-MG Capstone AFLR).

III. Steady RANS OAT15A Airfoil Simulations

Experimental coefficient of pressure (C_p) data at the Mach 0.73, Reynolds number 3×10^6, $\alpha = 2.5°$ condition was used to validate mesh and simulation parameters before attempting moving shock simulations. As described by Deck,[6] "at this angle of attack, a thin separated area exists at the foot of the shock, but no large-scale self-sustaining motion is observed experimentally." The lack of shockwave buffet simplifies comparison between the CFD predicted and experimentally measured airfoil pressure distributions. The results presented in the following subsections demonstrate that unstructured CFD methods are capable tools for studying steady transonic flowfields where SBLIs exist.

For steady RANS simulations the grid convergence index (GCI) was used to compare results among families of grids. It is defined[28] by:

$$GCI = \frac{F_s}{r^p - 1}\left|\frac{f_2 - f_1}{f_1}\right|, \tag{2}$$

where F_s is a factor of safety (3.0), r is the grid refinement factor previously discussed, p is the order of accuracy of the solver (2.0), f_1 is the finer grid solution, and f_2 is the coarser grid solution. The GCI results comparing C_l and C_d for the OAT15A families of grids are provided in Table 5. The $1/4\,cW$ family of grids demonstrate GCI values of approximately 1.9%, which means that the uncertainty in C_l and C_d are within 2% due to discretization. The $1/4\,cW$-wTEref and $3\,cW$ families of grids performed similarly, but trends could be better demonstrated by constructing grids with another level of refinement. The GCI values for the $3\,cW$ family of grids highlights notable differences in C_l and C_d due to trailing edge refinement. Based on the steady simulation predicted C_l and C_d, the finest grid is each family appears suitable for follow-on URANS analysis.

III.A. Predicted Steady Surface Pressures for Various Airfoil Meshes

Centerline airfoil pressure predictions from steady SA simulations utilizing very fine surface element size ($\Delta s = 0.02$") meshes of one-element, $1/12c$, and $1/4c$ span width airfoils are compared to S3Ch experimental data in Figure 2(a). The results show that the one-element width mesh (intended to represent an ideal 2-D airfoil), predicts a shock location closest to what was observed in the wind tunnel. As airfoil mesh width increases, the predicted shock location moves further aft but the agreement between predicted and measured C_p improves for $0.1 \le x/c \le 0.4$ on both the upper and lower surfaces. Therefore, it is difficult to conclude which mesh best represents the S3Ch test article based on these SRANS simulations alone.

Table 5. Grid convergence index (GCI) results for the families of OAT15A airfoil grids constructed. The aerodynamic coefficients are averaged over the last 100 iterations of a SRANS calculation with the SA turbulence model. Simulation conditions are Mach 0.73, Re_c=3×10^6, and α=2.5°.

Abbreviated Name	r	C_l	GCI_{C_l}	C_d	GCI_{C_d}
1/4 cW-M-airfoil	-	0.8214	-	0.0237	-
1/4 cW-F-airfoil	1.581	0.9134	20.16%	0.0286	34.29%
1/4 cW-VF-airfoil	1.539	0.9215	1.919%	0.0289	1.930%
1/4 cW-C-airfoil-wTEref	-	0.9018	-	0.0305	-
1/4 cW-M-airfoil-wTEref	1.149	0.9104	8.793%	0.0287	59.06%
3 cW-M-airfoil	-	0.8260	-	0.0241	-
3 cW-M-airfoil-wTEref	1.200	0.9126	64.40%	0.0290	115.2%
3 cW-F-airfoil	1.543†	0.8458	5.08%†	0.0248	6.63%†

† r, GCI_{C_l}, and GCI_{C_d} computed using N_2 and f_2 from 3 cW-M-airfoil grid

Predicted C_p profiles from simulations performed by Deck[6] utilizing 2-D structured grids are also shown in in Figure 2(a). Interestingly the FUN3D predictions that match most closely with Deck's CFD results, are not simulations using one-element wide grids, but those that utilize a 1/4 c span width 3-D grid with many spanwise elements. However, this finding provides confidence that unstructured CFD techniques are sufficient to predict shockwave oscillation onset conditions comparable to those observed by researchers using structured CFD methods.

Centerline airfoil surface C_p predictions from SRANS airfoil simulations utilizing grids with constant 1/4c span width and varying surface element size (Δs = 0.02", 0.04", 0.08") are presented in Figure 2(b). The steady SA simulation results using various size meshes show good agreement with top and bottom surface S3Ch pressure data, but predict a slightly aft shock location compared to the experiment. The steady SST simulation using the medium surface resolution mesh predicts a shock location closest to what was observed experimentally. It is interesting to note that large surface element size variations have a much smaller effect on the predicted airfoil surface pressure and shock location than airfoil mesh width or turbulence model used (Figure 2). These findings demonstrate that achieving grid convergence for transonic airfoil simulations with SBLI involves much more than simply increasing surface element resolution.

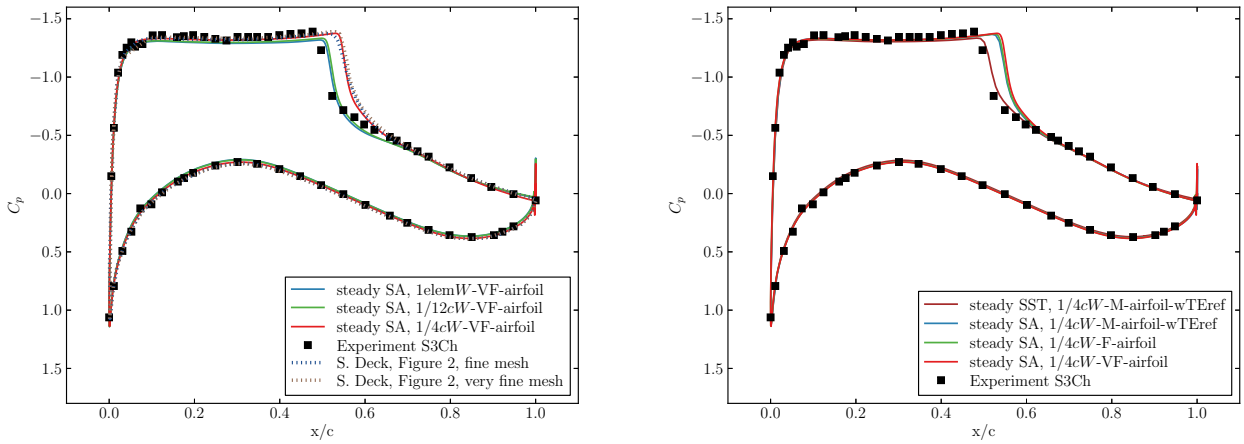

(a) varying span width OAT15A airfoil grids

(b) varying Δs, 1/4 c span width OAT15A airfoil grids

Figure 2. Steady RANS predicted OAT15A airfoil centerline C_p at Mach 0.73, Reynolds number 3×10^6, α = 2.5°, compared to S3Ch experiment data and CFD predictions by Deck.[6]

III.B. Predicted Lift from Steady RANS Simulations

An additional benefit of SRANS simulations is that the computations are at least an order of magnitude cheaper than URANS simulations. This advantage can be utilized to quickly explore the angle of attack regime where transonic shockwave oscillations might occur. Steady simulations for which large repeating variations in predicted lift and residuals occur, indicate unsteady simulations that can predict shockwave oscillations (but do not guarantee it). While this may seem trivial, since S3Ch wind tunnel tests indicate the α-range for which oscillations are expected for the OAT15A airfoil, using SRANS simulations for exploring the α-range is necessary for simulating other airfoil, wing, and aircraft models. Examples of these steady simulation predicted lift outputs are shown in Figure 3. The figure shows that predicted coefficient of lift (C_l) for the steady SA simulation at $\alpha = 2.5°$ has reached a converged value for over 4000 iterations, but oscillates for the entire duration at $\alpha = 3.5°$. Predicted C_l for the steady SST simulation at $\alpha = 2.5°$ takes some more iterations to reach a converged value, but overall SRANS results are similar for the both turbulence models. The SRANS lift predictions also suggest that airfoil mesh width and turbulence model may affect the magnitude of shock-buffet predicted by URANS simulations. However, URANS simulations are necessary to draw detailed conclusions regarding predicted shockwave oscillations due to SBLI.

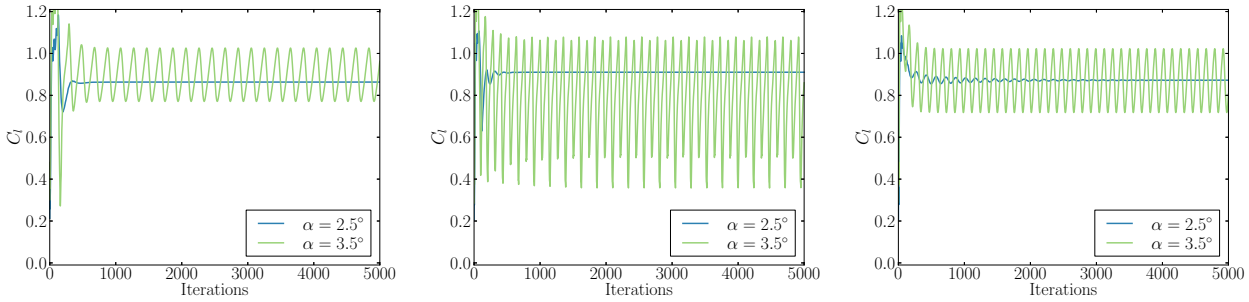

(a) steady SA, 1/12 cW-M-airfoil (b) steady SA, 1/4 cW-M-airfoil-wTEref (c) steady SST, 1/4cW-M-airfoil-wTEref

Figure 3. Predicted C_l from steady RANS simulations at $\alpha = 2.5°$ and $\alpha = 3.5°$ for select OAT15A airfoil grids.

IV. Unsteady RANS OAT15A Airfoil Simulations

Due to the time step and number of subiterations specified, each OAT15A URANS simulation required at least one week of wall-clock time in order to simulate enough physical time to characterize shockwave oscillation properties. The number of CPU-cores utilized for each simulation varied depending on mesh size and availability of computational resources. The FUN3D manual recommends using one CPU-core per 50,000 grid points.[25] For the simulations presented, no significant increase in simulation speed was observed for partitioning the grid beyond one CPU-core for every 20,000 grid points. Frequency and damping of the shockwave motion were analyzed by fitting simulation predicted C_l values to Equation 3.

$$L(t) = a_1 + a_2 e^{-a_3 t} \sin(a_4 t - t_0) \tag{3}$$

From the Equation 3 fit coefficients, the mean value was estimated using $\bar{L} = a_1$, peak-to-peak variation was estimated from a_2 via $\Delta L = 2a_2$, the damping coefficient (ζ) is calculated using a_3 via $\zeta = a_3/\sqrt{4\pi^2 + a_3^2}$, and frequency is calculated with a_4 via $f = a_4/2\pi$. The first 0.01 seconds of the time history was neglected in an attempt to minimize initial transient effects. While the temporal resolution of these simulations is relatively high, the time histories are too short to accurately measure low frequency content using an FFT approach.

All unsteady simulations were computed using a time step equivalent to 100 steps per advective timescale. An alternative approach would have been to decrease simulation time step with increasing surface grid resolution in order to keep time step with respect to grid spacing constant. While this would enhance comparison of simulations performed using different grids, it would also further increase the time required for unsteady simulations.

IV.A. Effect of Airfoil Mesh Width on URANS SA Predicted Oscillations

Unsteady RANS SA simulations using one-element, 1/12 c, and 1/4 c span width OAT15A airfoil grids were performed at the $\alpha = 3.5°$, freestream condition while keeping all CFD solver settings constant. The predicted C_l values from these simulations, shown in Figure 4 (a), demonstrated that airfoil mesh width has a significant effect on the magnitude and frequency of predicted shockwave oscillations. The ONERA work documented by Deck,[6] suggests that grids of at least 1/4 c-span width be used in order to capture low frequency three-dimensional mechanisms when simulating the OAT15A airfoil. While the ONERA researchers utilized zonal DES-based methods, the FUN3D results show that airfoil mesh width affects unsteady RANS model simulation results as well. Predicted C_l from simulations at $\alpha = 3.5°$, for 1/4 c span width OAT15A airfoil grids with and without trailing edge refinement are also presented in Figure 4, in order to contrast the effect to airfoil surface mesh size against airfoil grid width. The plots suggest that reducing surface element resolution results in lower amplitude oscillations at $\alpha = 3.5°$, and that trailing edge mesh refinement has a much greater effect on oscillations than surface mesh resolution.

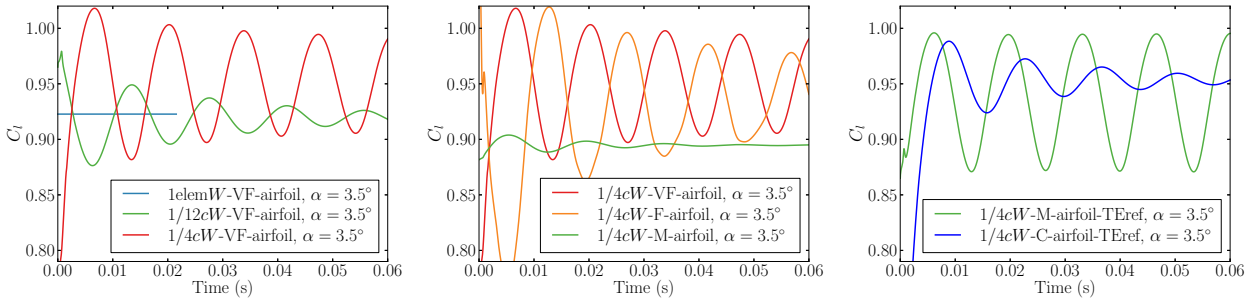

(a) various span width VF airfoil meshes (b) 1/4 cW airfoil meshes (c) 1/4 cW TEref airfoil meshes

Figure 4. Predicted C_l from unsteady SA FUN3D simulations at Mach 0.73, Reynolds number 3×10^6, $\alpha = 3.5°$, of various OAT15A airfoil meshes.

IV.B. Quarter-chord Width Airfoil Mesh URANS Results

Results from unsteady SA simulations using 1/4 c span width grids with varying airfoil surface element sizes, for the $3.5° \leq \alpha \leq 4.5°$ range at Mach 0.73, are presented in Figure 5. Results from unsteady SA and unsteady SST simulations for 1/4 c span width grids with trailing edge cell refinement for the same α and Mach conditions are shown in Figure 6. The frequency and damping characteristics of the predicted C_l oscillations from the various simulations calculated using Equation 3, are summarized in Table 6. These simulations show numerous trends, but challenge the researcher to draw any conclusions regarding mesh convergence.

As airfoil surface mesh resolution decreases, predicted mean C_l value decreases. Since the measured C_l value of the S3Ch test article for moving shock conditions is not known, it difficult to determine which mesh is better. The amplitude of predicted C_l oscillations is largest for medium mesh simulations. However since predicted oscillation amplitude is larger for the very fine mesh than the fine mesh, no definite trend exists.

The α at which C_l oscillations occur varies with the surface element size. Predicted oscillations at $\alpha = 3.5°$ are more strongly damped as surface element size increases. In contrast, oscillations at higher α values are more weakly damped as surface element size increases. This shift in α at which shock oscillations occur cannot be observed by only studying simulation results at a single α, as was presented in Figure 4. The frequency and damping of C_l oscillations with respect to α, varies the least for medium surface resolution ($\Delta s = 0.08in.$) mesh simulations.

For 1/4 cW-VF-airfoil mesh simulations, a strange behavior in C_l oscillations is noted for α=3.75° and α=4.0° at around t=0.04 seconds of simulated time. A visualization of the surface skin friction coefficient revealed that this shift in C_l frequency and mean value occurred when the predicted shockwave was not parallel to the leading edge for the entire airfoil span. The type effect was also observed later during simulations using the 3 c span OAT15A 3 cW-M-airfoil-wTEref and 1/4 c span NACA 64A204 1/4 cW-F-airfoil-wTEref meshes, and is visualized in Figures 8 and 13.

The addition of trailing edge cell refinement for the medium mesh had the greatest effect on predicted C_l values. This effect and the inducing trailing edge refinement are presented in Figure 6. Simulations using

this mesh showed sustained oscillations throughout the $3.5° \leq \alpha \leq 4.5°$ range. As noted in Table 6, the trailing edge refinement also caused the predicted shockwave oscillation frequency to shift ≈3 Hz for the medium surface mesh. Coarser surface mesh simulation results (Figure 6, bottom row) revealed that trailing edge refinement is not more important than airfoil surface cell sizes for URANS SBLI simulations.

Switching from the SA to SST turbulence model while using the same 1/4 cW-M-airfoil-wTEref mesh resulted in lower amplitude C_l oscillations for $3.5° \leq \alpha \leq 4.5°$. Predicted C_l plots for both simulations are shown in Figures 6(a) and (c). As shown in Table 6, frequency and damping of shockwave oscillations were also higher for SST simulations compared to SA simulations.

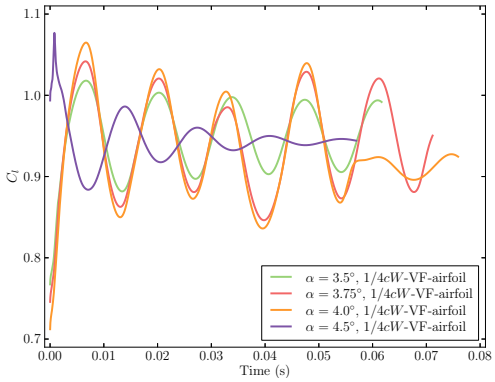

(a) unsteady SA predicted C_l

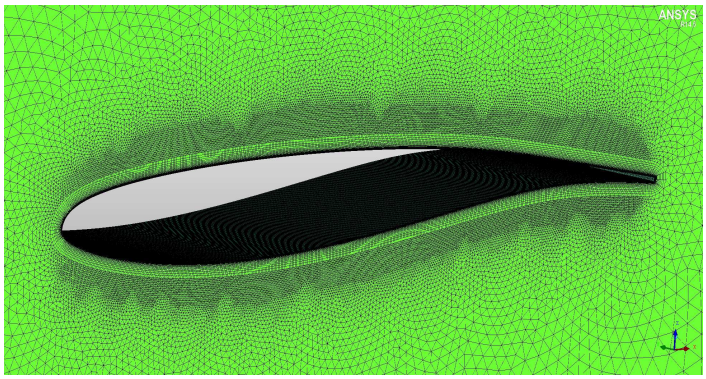

(b) 1/4 cW-VF-airfoil mesh

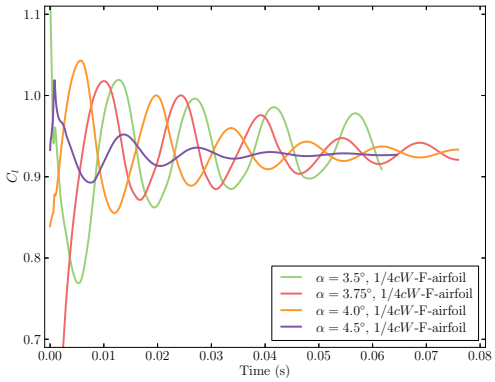

(c) unsteady SA predicted C_l

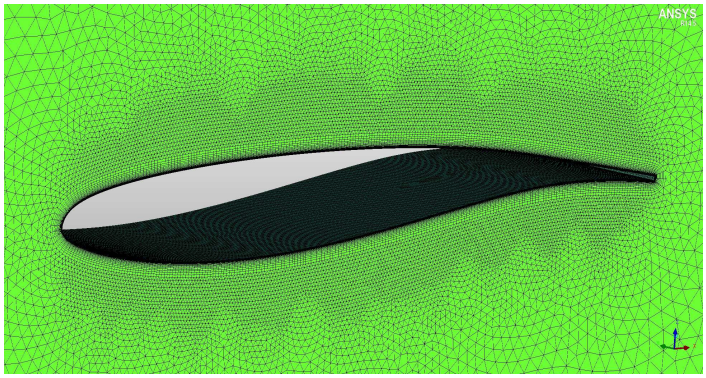

(d) 1/4 cW-F-airfoil mesh

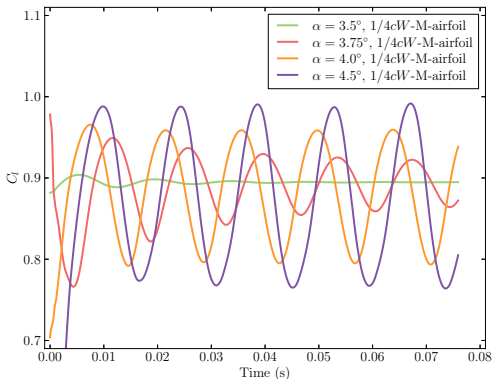

(e) unsteady SA predicted C_l

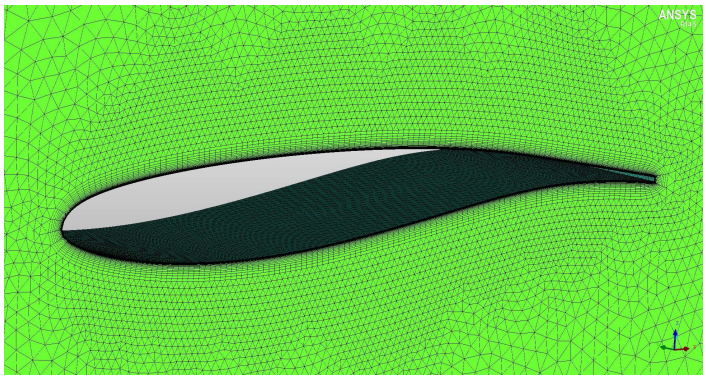

(f) 1/4 cW-M-airfoil mesh

Figure 5. Unsteady SA predicted C_l using OAT15A 1/4 c width airfoil meshes of varying surface element resolutions ($\Delta s = 0.02, 0.04, 0.08$ in.) for $3.5° \leq \alpha \leq 4.5°$ (left side), and images depicting meshes (right side).

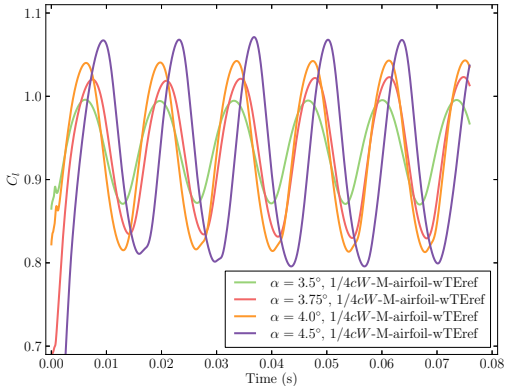

(a) unsteady SA predicted C_l

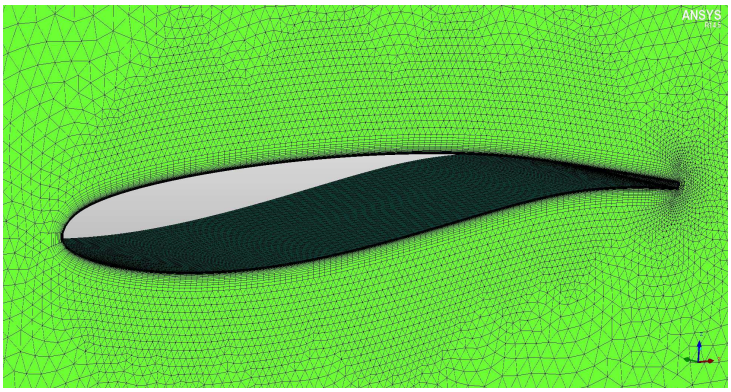

(b) 1/4 cW-M-airfoil-TEref mesh

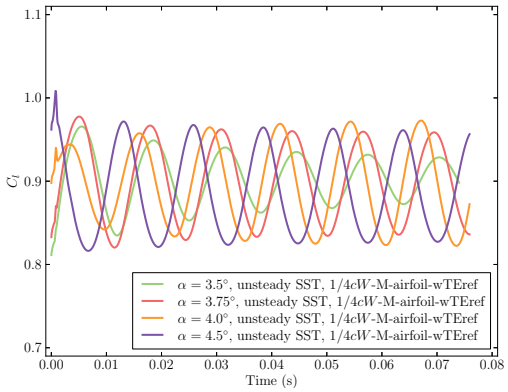

(c) unsteady SST predicted C_l

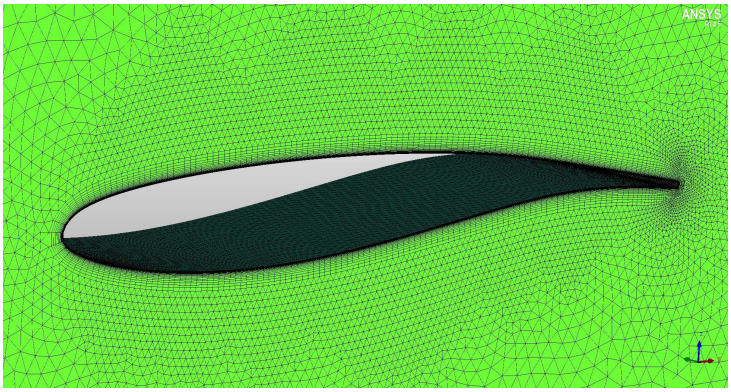

(d) 1/4 cW-M-airfoil-TEref mesh

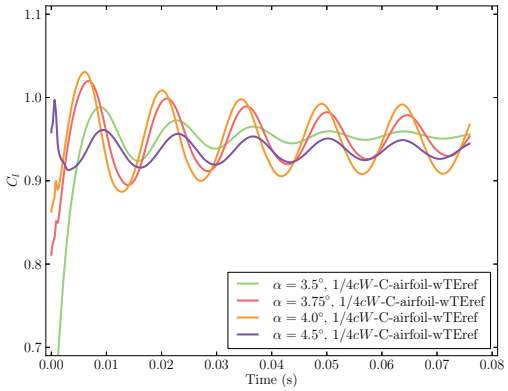

(e) unsteady SA predicted C_l

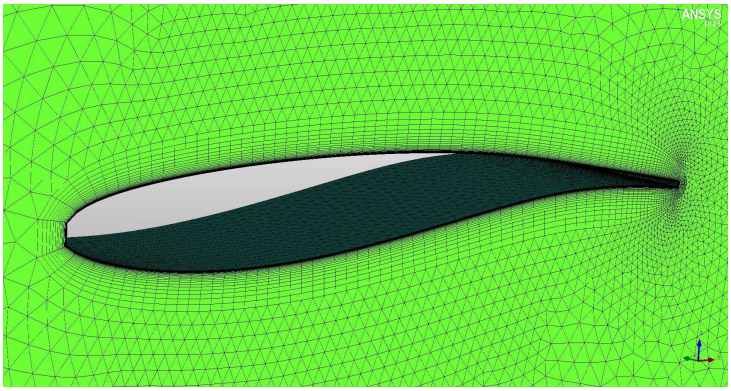

(f) 1/4 cW-C-airfoil-TEref mesh

Figure 6. URANS predicted C_l using OAT15A $1/4\ c$ width airfoil meshes with trailing edge refinement of varying surface resolutions ($\Delta s = 0.08, 0.16$ in.) for $3.5° \leq \alpha \leq 4.5°$ (left side), and images depicting meshes (right side).

Table 6. Frequency (f) and damping (ζ) values of URANS simulation predicted C_l oscillations using OAT15A $1/4\,c$ width airfoil meshes.

Simulation	α (deg.)	f (Hz)	ζ	Simulation	α (deg.)	f (Hz)	ζ
unsteady SA $1/4cW$-VF-airfoil	3.5	73.7	0.84	unsteady SA $1/4\,cW$-M-airfoil-TEref	3.5	74.3	-0.04
	3.75	≈ 73	-		3.75	74.2	-0.13
	4.0	≈ 74	-		4.0	72.5	-0.08
	4.5	74.0	0.995		4.5	73.8	0.05
unsteady SA $1/4\,cW$-F-airfoil	3.5	69.1	0.98	unsteady SST $1/4\,cW$-C-airfoil-TEref	3.5	77.2	0.85
	3.75	68.3	0.98		3.75	77.6	0.17
	4.0	70.3	0.99		4.0	78.2	-0.27
	4.5	74.7	0.996		4.5	78.7	0.33
unsteady SA $1/4\,cW$-M-airfoil	3.5	71.0	0.995	unsteady SA $1/4\,cW$-C-airfoil-TEref	3.5	72.7	0.989
	3.75	71.7	0.95		3.75	69.0	0.94
	4.0	71.0	0.01		4.0	69.0	0.87
	4.5	70.0	-0.08		4.5	73.8	0.91

* Properties of meshes are detailed in Table 2.

IV.C. Comparison of $3\,c$ and $1/4\,c$ Width Airfoil Mesh Unsteady SA Results

The difficult-to-predict nature of SBLI-induced oscillations is further demonstrated by URANS simulations with $3\,c$ span width airfoil meshes. These simulations predict irregular C_l oscillations that seem to damp out. Due to the increased computational expense of three-chord span width grids, simulations over the full α-range were only performed using the medium surface with trailing edge refinement mesh. This was the same surface discretization that yielded the best simulation results for $1/4\,c$ width OAT15A airfoil models. Figure 7 shows predicted C_l values for the two meshes of similar surface discretization but with different widths.

Plots of airfoil surface skin friction and Mach on a span-normal plane, comparing $1/4\,c$ and $3\,c$ width simulation results are presented in Figure 8. These plots illustrate predicted shockwaves at their most aft and forward locations, and also at a time when the shockwave is moving forward. The $3\,c$ width airfoil plots show that the erratic predicted C_l values are a result of the shockwave not remaining parallel to the leading edge over the entire $3\,c$ span airfoil. Unlike the 3-D shockwave effect observed in S3Ch experiments, CFD results show 3-D effects occurring about the airfoil mid-span. Comparing simulation surface visualizations to photos from the S3Ch experiment,[5] indicates that FUN3D unsteady SA simulations also predicted further aft shockwave locations than observed experimentally.

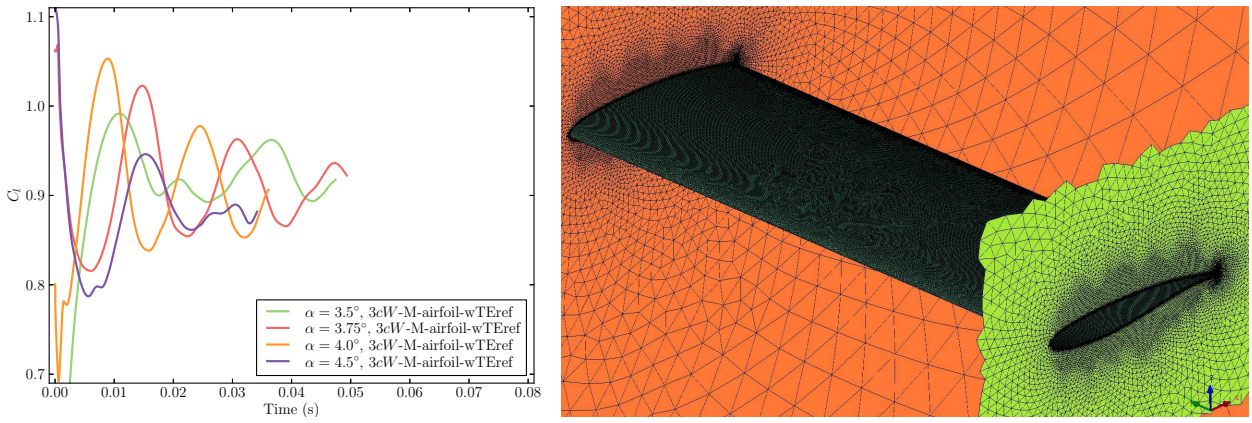

(a) predicted C_l for $3\,cW$-M-airfoil-TEref mesh

(b) $3\,cW$-M-airfoil-TEref mesh

Figure 7. OAT15A URANS simulation C_l predictions using $3\,c$ width airfoil mesh with trailing edge refinement for $3.5° \leq \alpha \leq 4.5°$ (left side), and image depicting mesh (right side).

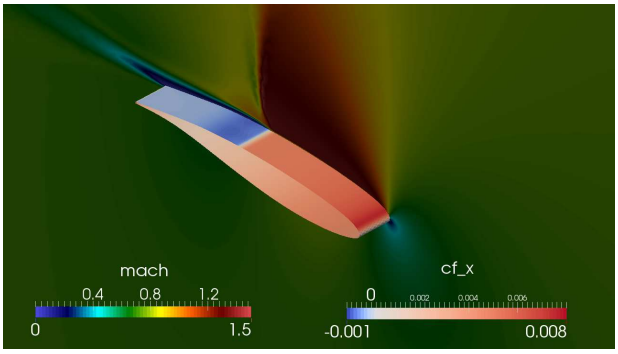

(a) t=0.021 sec; shock at aft most location; near max. C_l

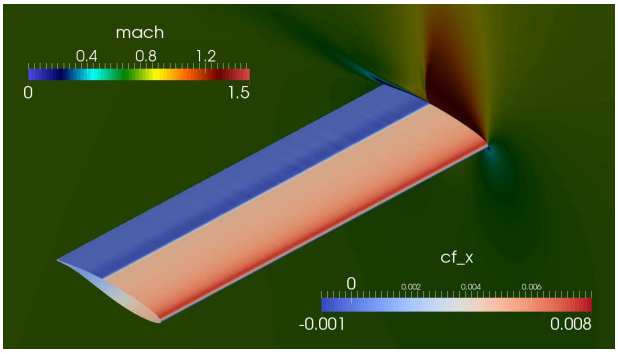

(b) t=0.011 s; shock at aft most location; near max. C_l

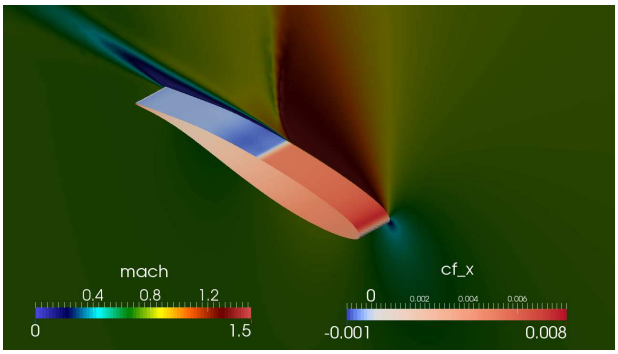

(c) t=0.027 sec; shock at forward most location; near min. C_l

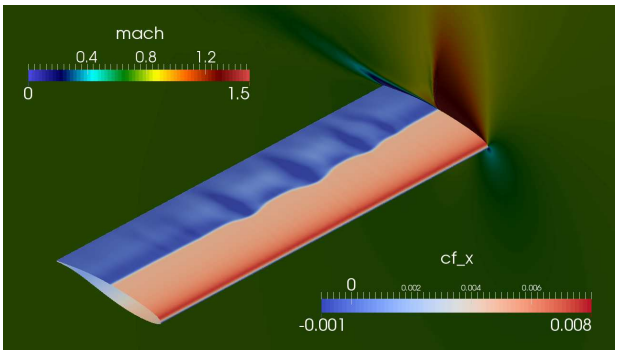

(d) t=0.019 sec; shock symmetrical about mid-span location but not parallel to leading edge; near local C_l min.

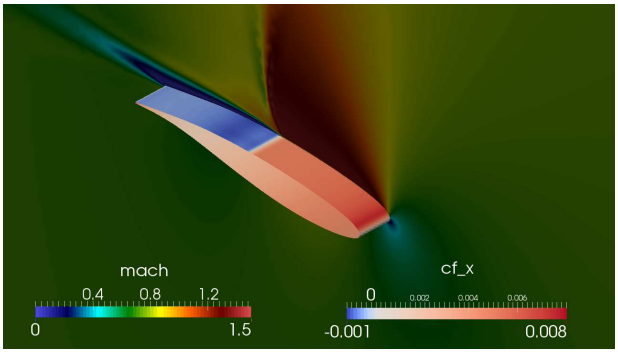

(e) t=0.038 s; shock moving forward; C_l decreasing

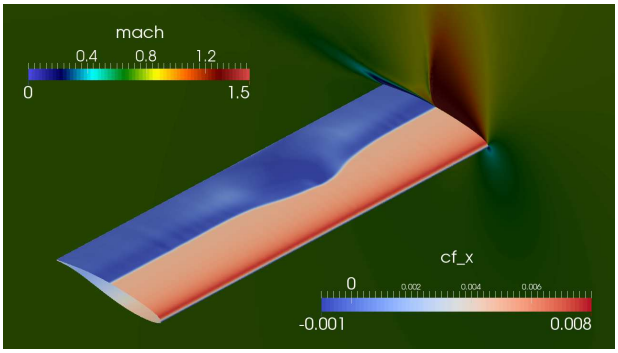

(f) t=0.042 sec; shock moving forward near mid-span location but not parallel to leading edge; C_l decreasing

Figure 8. Surface skin friction and cut-plane Mach visualizations, predicted by unsteady SA OAT15A airfoil simulations at Re_c=3×10^6, Mach 0.73, $\alpha = 3.5^\circ$ using $1/4\ cW$-M-airfoil-wTEref (left side) and $3\ cW$-M-airfoil-wTEref (right side) grids.

IV.D. Airfoil Surface Pressure and Skin Friction Temporal Analysis

The plots in Figures 9 and 10, present an alternate way to observe how the pressure coefficient (C_p) and streamwise skin friction coefficient ($C_{f,x}$) evolve on the OAT15A airfoil surface over time. In Figure 9, C_p and $C_{f,x}$ contours are plotted against chord location (x) and time along the center-line for the unsteady SA simulation at $\alpha = 3.5°$ using $1/4\ cW$-M-airfoil-TEref mesh. On the top surface C_p plot (Figure 9 a), the shockwave travel distance and oscillation period can be easily measured. Notable oscillations are also seen in the bottom surface C_p plot (Figure 9 b), even in the absence of a shockwave directly on the surface. This indicates that top-surface pressure waves do influence the C_p distribution on the bottom airfoil surface. Also in Figure 9, $C_{f,x}$ along the top and bottom surface centerlines are plotted against chord location (x) and time. On the top surface plot (Figure 9 c) evidence of separation and reattachment downstream of the shockwave are easily visualized. The bottom surface $C_{f,x}$ plot (Figure 9 d) also shows periodic variations aft of the shock location, and slightly upstream of where periodic variations are observed of the bottom surface C_p plot (Figure 9 b).

In Figure 10, centerline $C_{f,x}$ contours are plotted for the unsteady SST simulation at $\alpha = 3.5°$ using the $1/4\ cW$-M-airfoil-TEref mesh. The top surface plot clearly shows how quickly the shockwave movement damps out compared to the SA simulation. The plot also shows that forward shock location remains unchanged but that shockwave travel distance is significantly reduced when the SST turbulence model is used. The reduced shock travel shown in the $C_{f,x}$ contour plot is consistent with the higher frequency of oscillations predicted by unsteady SST simulations noted in Table 6.

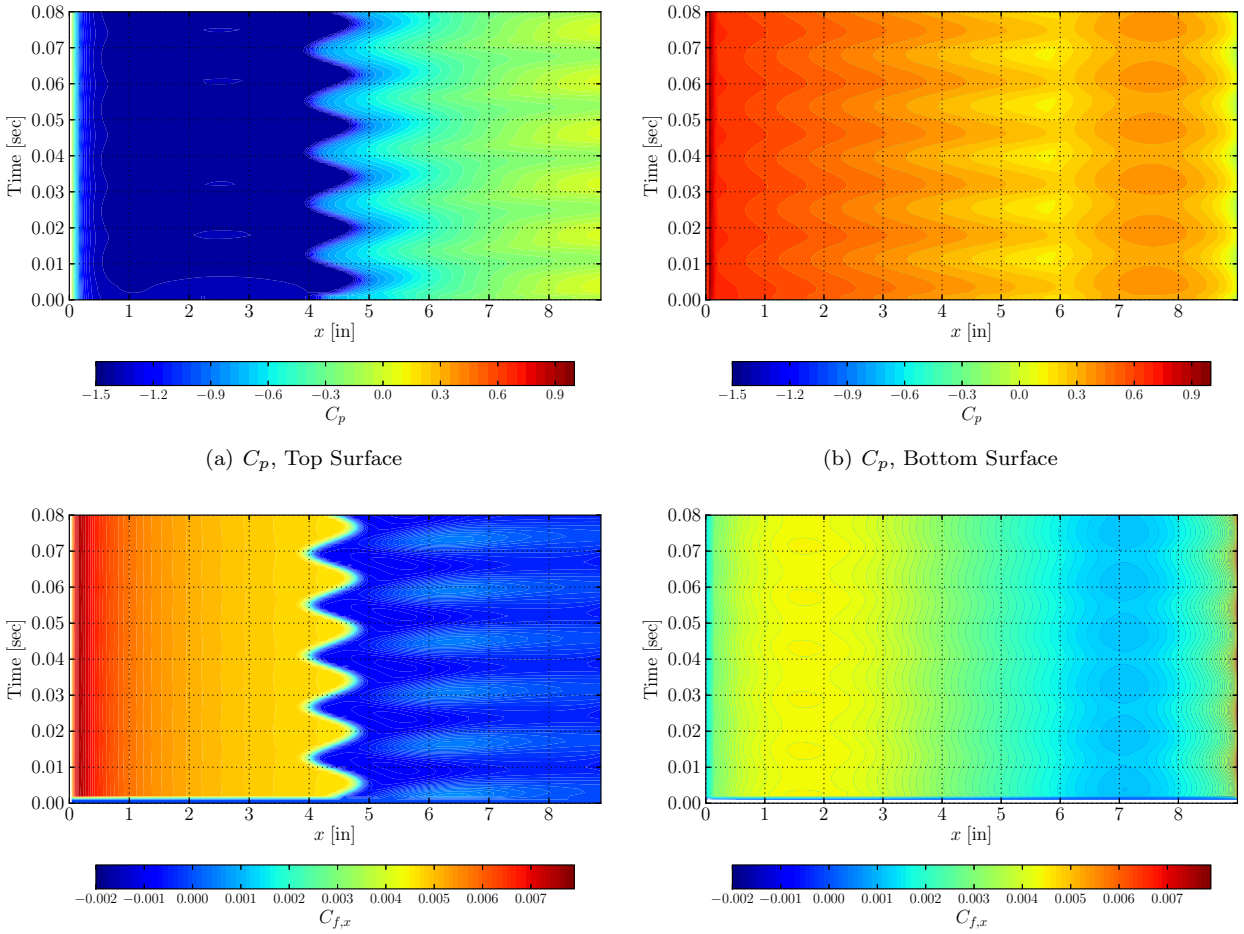

(a) C_p, Top Surface

(b) C_p, Bottom Surface

(c) $C_{f,x}$, Top Surface

(d) $C_{f,x}$, Bottom Surface

Figure 9. OAT15A centerline pressure coefficient, C_p, and skin friction coefficient, $C_{f,x}$, contours plotted against time and chord for unsteady SA simulation at Re_c=3×10^6, Ma=0.73, $\alpha = 3.5°$ using $1/4\ cW$-M-airfoil-TEref mesh.

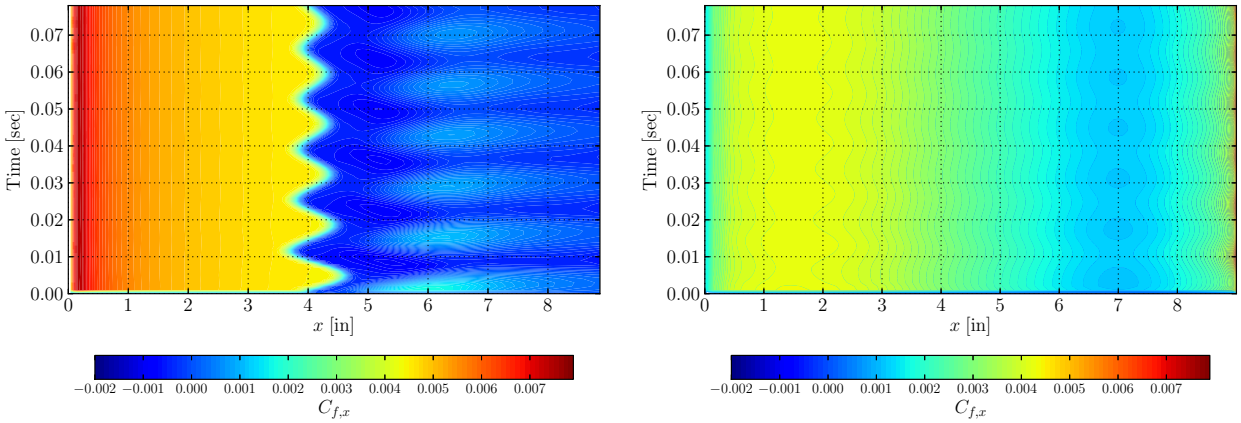

(a) $C_{f,x}$, Top Surface

(b) $C_{f,x}$, Bottom Surface

Figure 10. OAT15A centerline pressure coefficient, C_p, and skin friction coefficient, $C_{f,x}$, contours plotted against time and chord for unsteady SA simulation at Re_c=3×10^6, Ma=0.73, $\alpha = 3.5°$ using $1/4\,cW$-M-airfoil-TEref mesh.

V. NACA 64A204 Airfoil Simulations

The NACA 64A204 airfoil was simulated at the Mach 0.75, 5,000 and 33,000 feet pressure altitude freestream conditions. This corresponds to Reynolds numbers of 24×10^6, and 10×10^6 respectively. The α-range simulated ($3.5° \leq \alpha \leq 7.5°$) was chosen based on the previous simulation work performed by the authors and other researchers in the field.[10,17] The timesteps specified for unsteady simulations (6.28×10^{-5} and 6.28×10^{-6} seconds) corresponded to 100 and 1000 steps per advective scale respectively. Only $1/4c$ width airfoil meshes were utilized. Previous research efforts[10,17] have shown that the NACA 64A204 experiences shock-buffet at a frequency of approximately 8 Hz at the specified conditions.

V.A. Steady SA Results

Based on the lessons learned from OAT15A airfoil simulations, steady SA simulations of the NACA 64A204 airfoil were performed to explore angle of attack and mesh resolution for which shockwave oscillations might be predicted. Results of steady simulations using the $1/4\,cW$-M-airfoil-wTEref grid are presented in Figure 11 (a). The predicted lift force output shows that the airfoil is in fact operating in the post-stalled regime for $\alpha > 3.5°$, where transonic shockwave oscillations are expected. However, the steady simulation lift values converge over the entire $3.5° \leq \alpha \leq 7.5°$ range. This behavior suggests that the medium resolution NACA 64A204 airfoil grid is insufficient to simulate shockwave oscillations. Results of steady simulations with the $1/4\,cW$-F-airfoil-wTEref grid are presented in Figure 11 (b). For the finer surface NACA 64A204 grid, sustained oscillations are observed at the α=4.5° and 5.5° conditions.

The effect of greater volume element density was studied by utilizing fine surface resolution grids with fluid element global size increments smaller than 1.1. Steady SA simulation results using the $1/4\,cW$-F-airfoil-wTEref-gsi1.05 NACA 64A204 airfoil grid (Figure 11 c) show that changing global mesh resolution independent of the surface mesh resolution affects whether shockwave oscillations are predicted. While this may be intuitively congruent for coarser meshes, it is surprising to observe that finer volume grid simulations can fail to predict oscillations as well.

The GCI results comparing C_l and C_d for the NACA 64A204 airfoil family of grids are provided in Table 7. C_l and C_d for GCI calculations are obtained from unsteady RANS simulations at α=3.5°. At this condition, no unsteady features were predicted regardless of grid or simulation parameters utilized. The $1/4\,cW$ family of grids demonstrate GCI values of <1% which demonstrates that the uncertainty in C_l and C_d for follow-on analysis will likely be due to factors other than discretization error. The steady simulation behavior highlighted in Figure 11 demonstrates that the medium grid and fine grid with increased volume density, are not suitable for follow-on analysis. The authors deem only the $1/4\,cW$-F-airfoil-wTEref grid appropriate for URANS simulations.

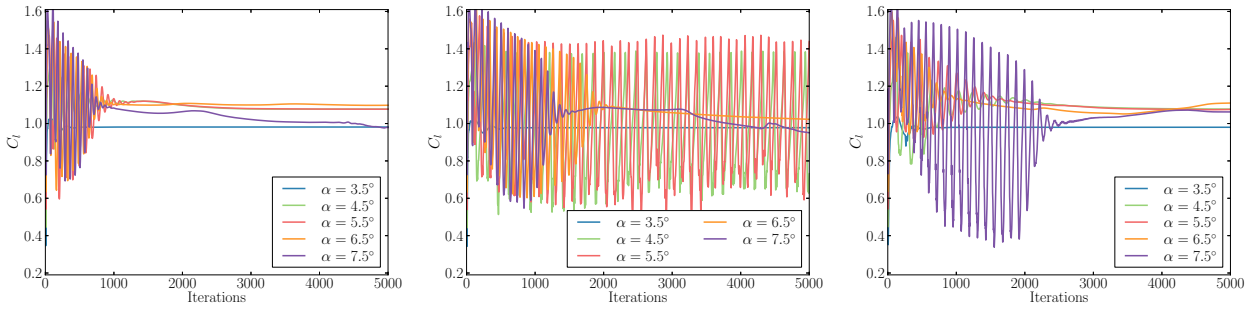

(a) 1/4 cW-M-airfoil-wTEref (b) 1/4 cW-F-airfoil-wTEref (c) 1/4 cW-F-airfoil-wTEref-gsi1.05

Figure 11. Steady SA simulation predicted C_l for $\alpha = 3.5° - 7.5°$ using 1/4 c width NACA 64A204 airfoil meshes.

Table 7. Grid convergence index (GCI) results for the family of NACA64A2014 airfoil grids constructed. The aerodynamic coefficients are averaged over the last 100 iterations of a SRANS calculation with the SA turbulence model. Simulation conditions are Mach 0.75, Re_c=24×10^6, and α=3.5°.

Abbreviated Name	r	C_l	GCI_{C_l}	C_d	GCI_{C_d}
1/4 cW-M-airfoil-wTEref	-	0.9814	-	0.0276	-
1/4 cW-F-airfoil-wTEref	1.176	0.9778	2.824%	0.0275	5.633%
1/4 cW-F-airfoil-wTEref-gsi1.05	1.090	0.9801	3.723%	0.0275	2.745%
1/4 cW-F-airfoil-wTEref-gsi1.02	1.316	0.9792	0.381%	0.0274	0.897%

V.B. Unsteady RANS Results

Unsteady SA and SST simulations using the 1/4 cW-F-airfoil-wTEref grid failed to predict sustained shock-wave oscillations. Based on steady simulation results presented in the previous section, oscillations were expected at $\alpha = 4.5°$ and 5.5°. The predicted lift force, shown in Figure 12, damps out very quickly and achieves a steady value after $t = 0.25$ seconds, for all conditions simulated. Simulations using an order of magnitude smaller timestep were attempted, but demonstrated that timestep was not a significant factor in the results observed. Unsteady SST simulations at two different Reynolds number conditions also yielded similar results at $\alpha = 4.5°$ and 5.5°.

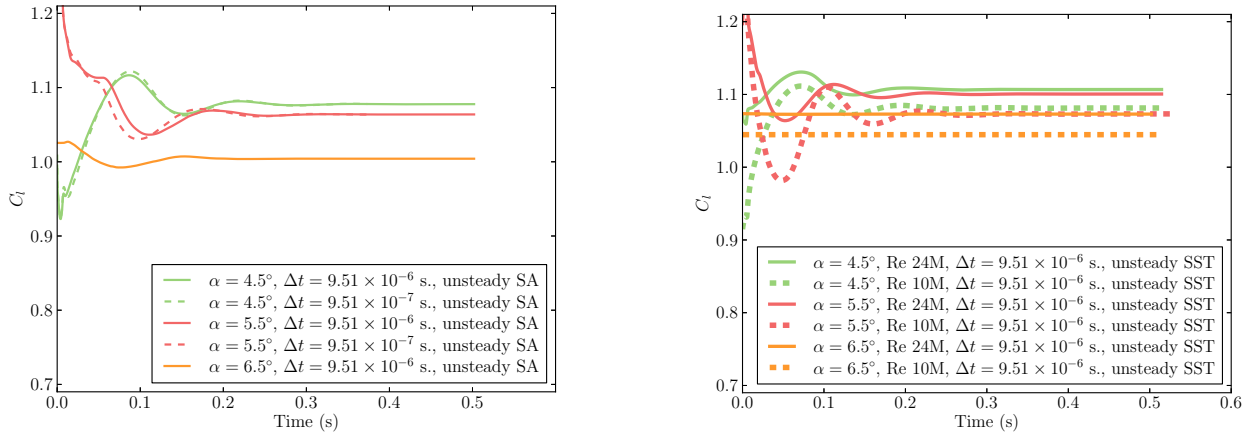

(a) unsteady SA, for two Δt simulated (b) unsteady SST, for two Re numbers simulated

Figure 12. Unsteady RANS predicted C_l for $\alpha = 4.5° - 6.5°$ using NACA 64A204 1/4 cW-F-airfoil-wTEref mesh.

Surface skin friction plots from the unsteady SA simulation at $\alpha = 5.5°$ are presented in Figure 13. The plots highlight a potential cause for the lack of sustained shock-buffet. A spanwise irregularity is observed in the predicted shockwave. The shockwave irregularity appears symmetrical at beginning of the simulation ($t = 0.006$ s.), but quickly settles to a non-symmetrical shape. Some shockwave movement does occur, but predicted shock location converges to a position in between the aft-most location observed at $t = 0.05$ s.

(Figure 13 b), and the forward-most location observed at $t = 0.10$ s (Figure 13 c). Surface skin friction plots from the unsteady SST simulation at $\alpha = 5.5°$, shown in Figure 14), do not demonstrate strong spanwise shock irregularity. However they do not show significant shockwave movement either. Once again aft-most location is observed at $t = 0.05$ s. (Figure 14 b), and the forward-most location observed at $t = 0.10$ s. (Figure 14 c). The coverged shock location, at $t = 0.05$ s (Figure 14 d), is at a position in between the forward-most and aft-most locations observed.

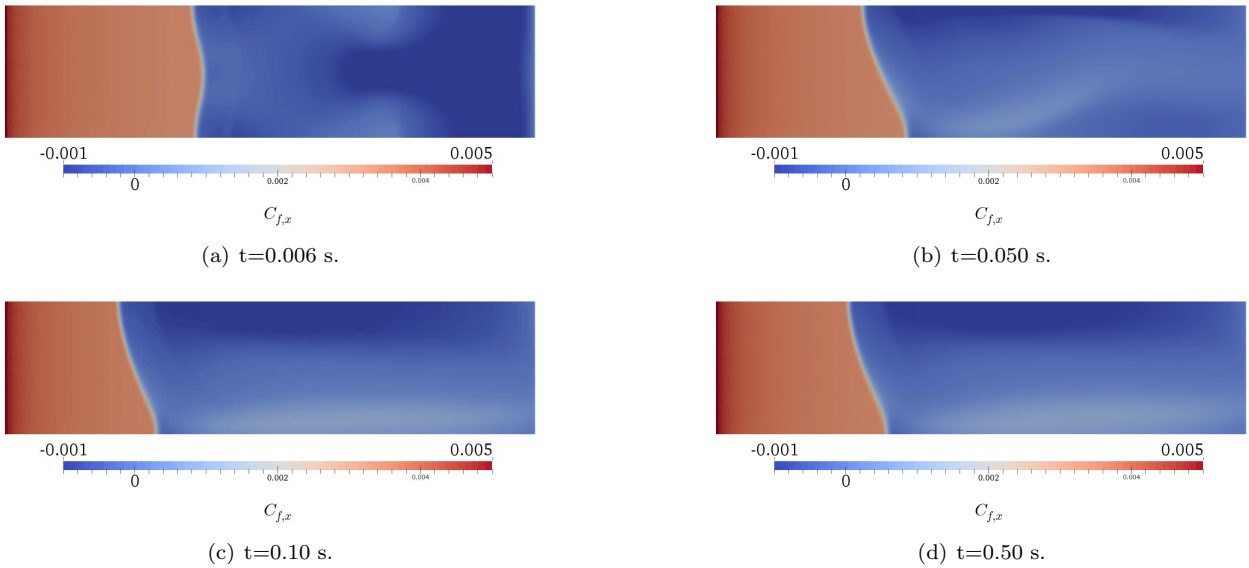

(a) t=0.006 s. (b) t=0.050 s.

(c) t=0.10 s. (d) t=0.50 s.

Figure 13. Visualization of $C_{f,x}$ predicted by unsteady SA simulation at $Ma = 0.75$, $Re_c = 24 \times 10^6$, $\alpha = 5.5°$ using NACA 64A204 $1/4\,cW$-F-airfoil-wTEref mesh

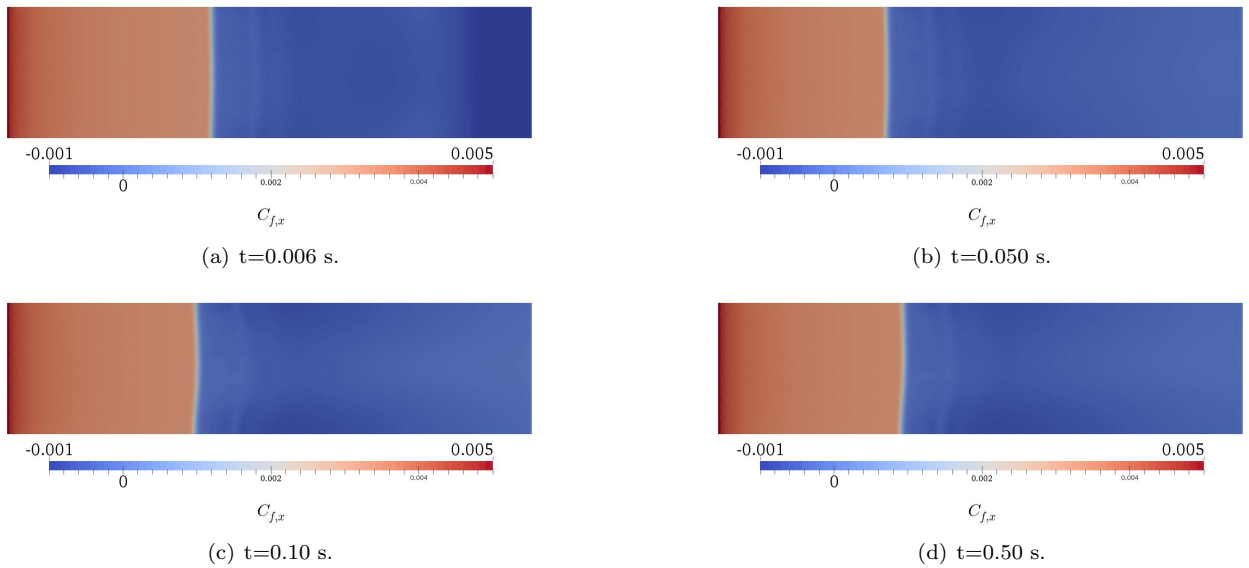

(a) t=0.006 s. (b) t=0.050 s.

(c) t=0.10 s. (d) t=0.50 s.

Figure 14. Visualization of $C_{f,x}$ predicted by unsteady SST simulation at $Ma = 0.75$, $Re_c = 24 \times 10^6$, $\alpha = 5.5°$ using NACA 64A204 $1/4\,cW$-F-airfoil-wTEref mesh

V.C. Contrast to Previous Unsteady SA Research Results

The results in this subsection are from the authors' NACA 64A204 airfoil unsteady SA simulation research previously presented at the 12th U.S. National Congress on Computational Mechanics. Results from a single simulation at Re_c=24×10^6, Mach 0.75, $\alpha = 5.5°$, are shown to demonstrate differences in flowfield characteristics between simulations that predicted shockwave oscillations, and those that did not. Numerous

grid topology and flow solver differences exist between the results presented below and the URANS results presented in the rest of paper. A key grid difference is the width of the airfoil grid utilized. Previous airfoil simulations utilized 1-element width meshes, while the current research was performed using $1/4\,c$ width meshes. The reader is referred to the previously published work[17] for further grid and flow solver details.

Compared to $1/4cW$-F-airfoil-wTEref mesh unsteady SA results (Figure 13), 1-element width airfoil simulations predicted a forward shock location that was much closer to the airfoil leading edge. A visualization of flowfield density gradient from the unsteady SA simulation utilizing a 1-element width grid is shown in Figure 15. The flowfield snapshots at four instances during the shockwave oscillation cycle are presented. Figures 15 (b) and 15 (d) both show the shockwave at the midpoint of its travel extents. However, significant differences in shockwave shape, and boundary layer separation region aft of the shockwave exist depending on which direction the shock is traveling. The top and bottom surface C_p contour plots in Figure 16 show the shockwave travel distance is approximately 20 inches, occurs ahead of the mid-chord location, and that the bottom airfoil surface experiences strong pressure fluctuations as well.

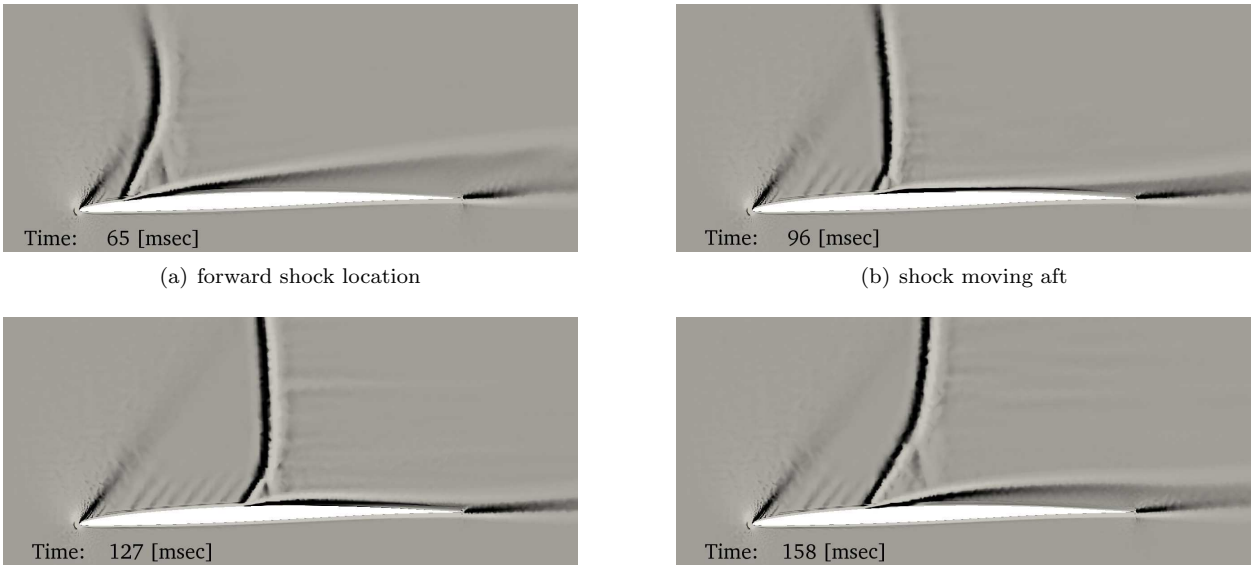

(a) forward shock location

(b) shock moving aft

(c) aft shock location

(d) shock moving forward

Figure 15. Visualization of flowfield density gradient from authors' earlier unsteady SA simulation work[17] utilizing NACA 64A204 1-element wide airfoil at Re_c=24×10^6, Ma=0.75, $\alpha = 5.5°$

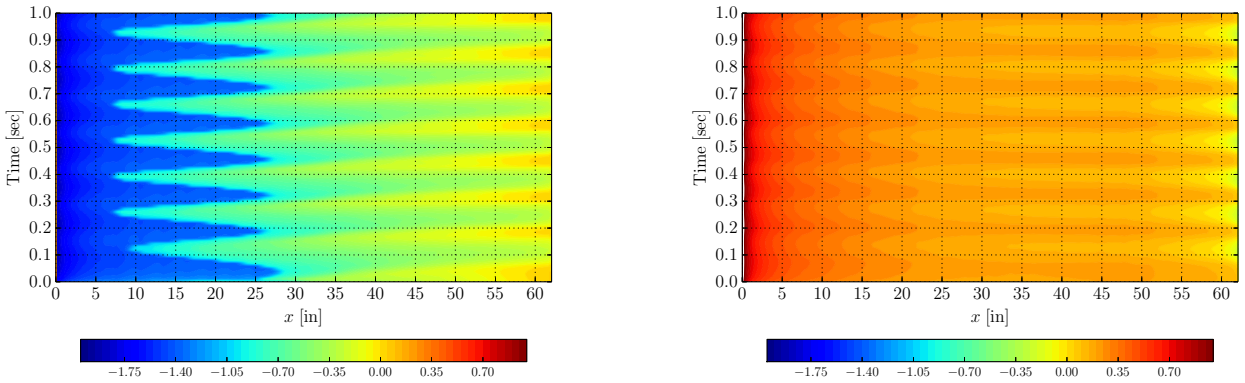

(a) C_p, Top Surface

(b) C_p, Bottom Surface

Figure 16. NACA 64A204 1-element wide airfoil pressure coefficient, C_p contours plotted against time and chord from authors' earlier unsteady SA simulation work[17]at Re_c=24×10^6, Ma=0.75, $\alpha = 5.5°$.[17]

VI. Non-Airfoil Geometry Simulation Results

Select non-airfoil geometry simulation results are presented in the following section. These simulations highlight flowfield behavior that may be encountered when simulating shockwave oscillations on an F-16 aircraft with stores. Lessons learned from airfoil simulations were utilized to guide the model building and simulation processes applied.

VI.A. One-element Width OAT15A Airfoil with 2-D Store Geometry

Initial OAT15A airfoil simulations utilized one-element wide meshes to facilitate the testing of FUN3D solver settings at minimum computational cost. However, the one-element wide meshes did not predict sustained oscillations regardless of angle of attack simulated, or time step, subiterations, or time integration method employed. Steady SA simulation predicted C_l over the wind tunnel tested α-range, Figure 17 (a), showed no oscillation behavior even though results indicated the airfoil was in the post-stall regime. This was perplexing, considering that the one-element wide steady SA simulation predicted a shock location closest to the experiment (see Figure 2 a) at $\alpha = 2.5°$. Attempts to initiate shockwave movement in unsteady simulations by pitching the airfoil by $\pm 1°$, or starting unsteady simulations using a steady solution from a simulation at a higher α, did not result in URANS simulations that predicted sustained shockwave oscillations. Time histories of predicted C_l from these one-element wide mesh unsteady SA simulations are shown in Figure 17 (b).

This steady flowfield predicted by numerical simulations changed completely when a 2-D store-like geometry was added beneath the airfoil. The size and location of the 2-D store was chosen to be similar to stores normally carried on aircraft wings, but the shape is a rectangle with triangular tip as opposed to a specific store profile. The spanwise grid width (1 element), surface element size (Δs=0.02 in), and FUN3D solver settings were unchanged. Large undamped C_l oscillations at 68 Hz (Figure 17 c) and significant shockwave movement were observed in unsteady SA simulations at the same Mach 0.73, $\alpha = 3.5°$ condition. Smaller oscillations also present in the URANS predicted C_l occur at frequency of approximately 2000 Hz, and correspond to the Strouhal number of the store-like geometry. It is interesting to note that the main frequency of predicted C_l oscillations closely matches the frequency of shockwave oscillations observed in S3Ch OAT15A experiments, even with the more chaotic store-induced flowfield.

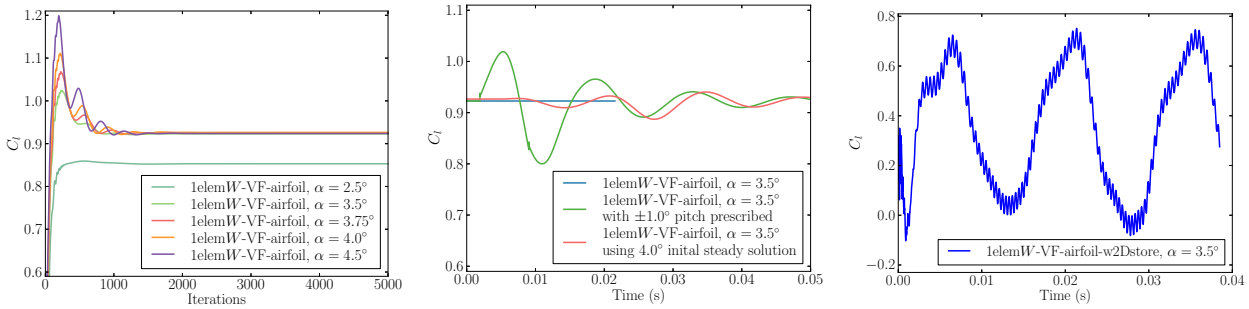

(a) steady SA predicted C_l (b) unsteady SA predicted C_l (c) unsteady SA predicted C_l

Figure 17. Steady SA and unsteady SA predicted C_l at Mach 0.73 for very fine surface resolution (Δs=0.02 in.=1/450c) one-element wide OAT15A airfoil, and airfoil with 2-D store geometries.

Mach visualizations of the unsteady SA predicted flowfields with the airfoil (1elem$W$-VF-airfoil) and airfoil with 2-D store (1elem$W$-VF-airfoil-w2Dstore) meshes are presented in Figure 18. The predicted upper surface aft shock location (Figure 18 c) did not change significantly compared to the airfoil only geometry (Figure 18 a). However, the predicted upper surface forward shock location ((Figure 18 b) is closer to the airfoil leading edge than anything observed during wind tunnel testing. Predicted average C_l is significantly lower than the airfoil only case, and consistent with higher speed bottom surface flow due to the channel effect generated by the 2-D store. The presence of the 2-D store also generates a shock on the bottom airfoil surface. Visualization suggests this shockwave generates a region of separated flow underneath the airfoil (depicted by blue-colored regions in Figure 18). It is observed that the amount of separated flow aft of the upper surface shockwave is also much larger when the 2-D store is present. Determining whether the the large upper surface shockwave oscillations are caused by the store geometry introducing more grid points

below and aft of the airfoil, producing a shockwave on the airfoil bottom surface, or originating unsteady flow requires further investigation.

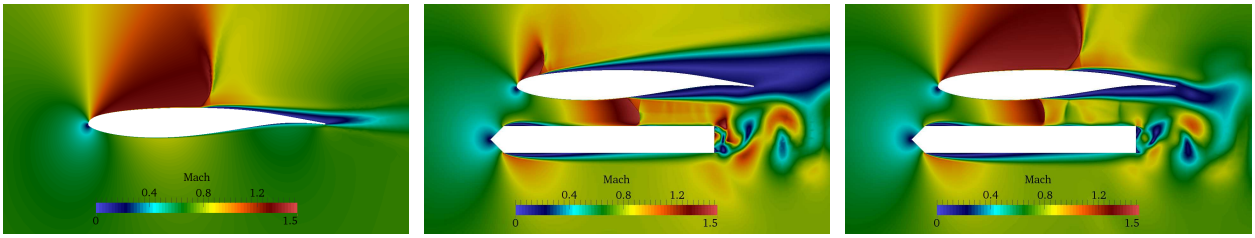

(a) fixed shock location; t=0.02 s. (b) forward shock location; t=0.0277 s. (c) aft shock location; t=0.0356 s.

Figure 18. Mach visualization of unsteady SA predicted flowfields at Mach 0.73, $\alpha = 3.5°$ for very fine surface resolution (Δs=0.02 in.=1/450 c) one-element wide OAT15A airfoil (left), and airfoil with 2-D store (center, right) geometries.

VI.B. OAT15A Wing with Tip-launcher-representative Geometry

An OAT15A airfoil-based wing with tip-launcher-representative geometry grid (3cW-M-wing-wTEref-wTipL) was also constructed. A picture of this grid is shown in Figure 19 (a). This model allowed the researchers to apply the lessons learned, and studying shockwave oscillations on the type of 3-D geometry that is generally targeted by unstructured grid simulation methods. A medium surface element size (Δs=0.08 in.=1/112.5 c) and trailing edge cell refinement were specified on the wing surface. In order to minimize changes between simulations using the numerous grids, a symmetry boundary condition was specified at the wall coincident with the wing root.

Once again, the process of using steady SA simulations to explore the α-range for predicted oscillations was employed. The steady SA simulation results, Figure 19 (b), showed that oscillations could be expected at the $\alpha = 5.5°$, and $6.0°$. Unsteady SA simulations were performed at both of these α conditions. Predicted C_l from the URANS simulations are shown in Figure 19 (c). The irregular variations seen in the plot indicate that 3-D shockwave effects are likely present. The unsteady SA oscillations predicted at $\alpha = 6.0°$ occur at approximately 64 Hz and have a damping coefficient close to zero, once the initial irregularities settle out.

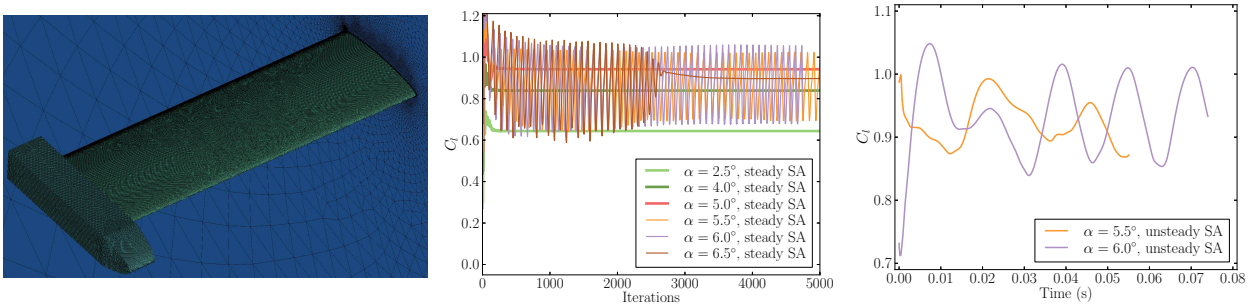

(a) 3 cW-wing-wTEref-wTipL mesh (b) steady SA predicted C_l (c) unsteady SA predicted C_l

Figure 19. OAT15A wing with tip-launcher-representative geometry and FUN3D simulation results at Mach 0.73.

Snapshots of the streamwise surface skin friction coefficient ($C_{f,x}$) visualization over time, from the unsteady SA simulation at $\alpha = 6.0°$ are presented in Figure 20. The figure shows that the majority of the shockwave movement occurs on the inboard half of the wing. The predicted shock location at the wing tip does not change throughout the entire duration of the unsteady simulation. However the inboard portion of shock the does not remain parallel to the leading edge. Spanwise irregularities of the inboard shock and spanwise $C_{f,x}$ aft of the shockwave, correspond to irregularity in predicted C_l (Figure 19 c). This is demonstrated by the snapshots at $t = 0.014, 0.030, 0.04s$, and 0.071 seconds in Figure 20. Spanwise shock and $C_{f,x}$ irregularities are at a minimum when predicted C_l is at a local maximum ($t = 0.007, 0.039, 0.055$, and 0.071 seconds). The root cause of the strange shockwave motion, and the effect of the symmetry boundary condition at the wing root wall requires further investigation.

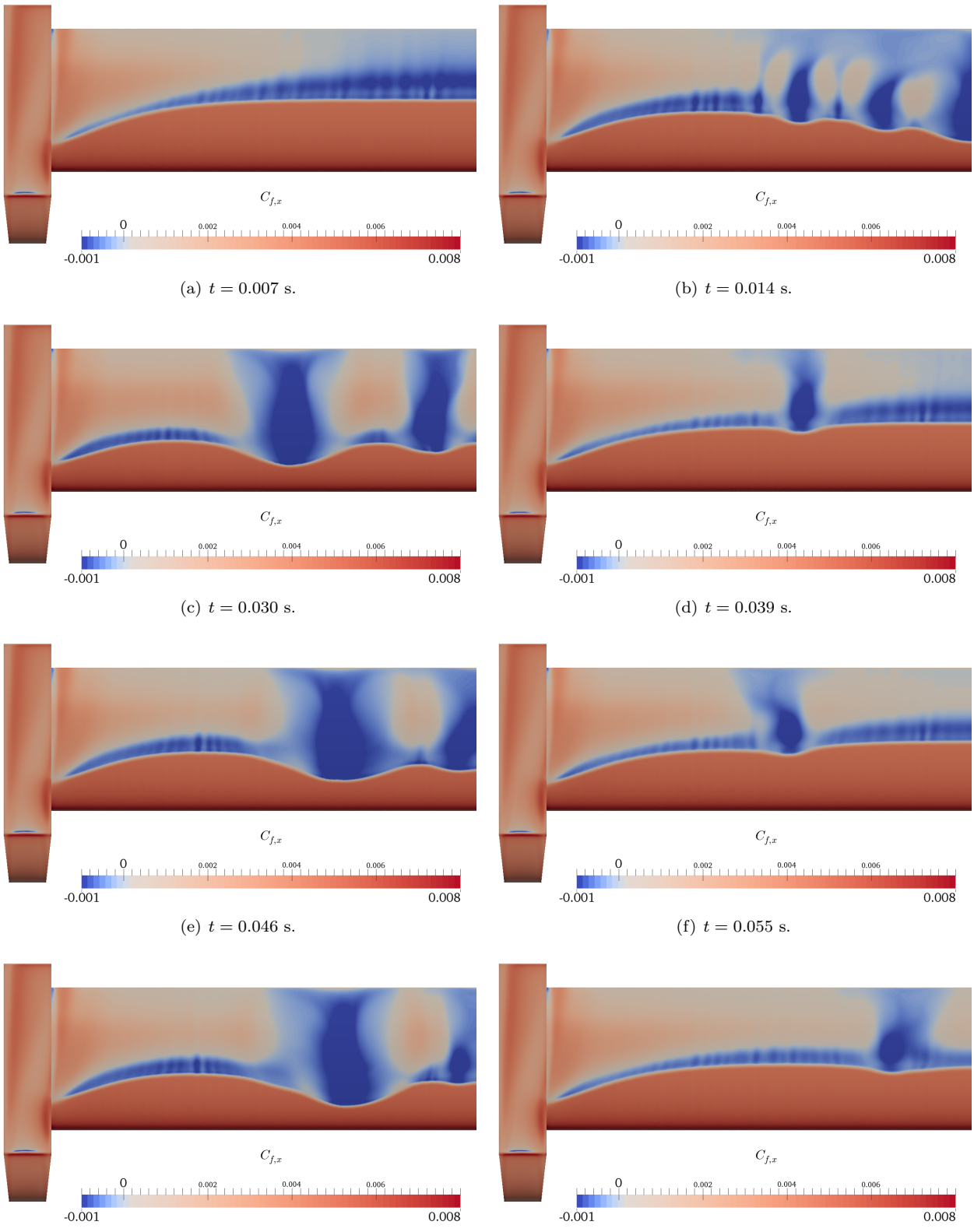

(a) $t = 0.007$ s. (b) $t = 0.014$ s.

(c) $t = 0.030$ s. (d) $t = 0.039$ s.

(e) $t = 0.046$ s. (f) $t = 0.055$ s.

(g) $t = 0.063$ s. (h) $t = 0.071$ s.

Figure 20. Streamwise surface skin friction ($C_{f,x}$) visualization for wing with tip-launcher-representative geometry predicted by unsteady SA OAT15A simulation at Mach 0.73, $\alpha = 6.0^\circ$.

VII. Conclusions

The OAT15A and NACA 64A204 airfoil simulation results are promising but also demonstrate the difficultly of predicting transonic shock-buffet resulting from SBLI. Steady RANS simulations are incredibly useful for narrowing down grid requirements to simulate shockwave oscillations, and quickly explore the α-range where the oscillations occur. However, even on a simple airfoil model, URANS predicted shockwave oscillations were sensitive to the width of the grid used, surface cell size, and cell refinement away from the shockwave. For the OAT15A unsteady SA simulations performed, many different grids predicted oscillations around the 70 Hz frequency observed in S3Ch OAT15A airfoil experiments, but only one grid predicted sustained oscillations for the entire 3.5° to 4.5° α-range. Simulations utilizing OAT15A airfoil with 2-D store and OAT15A wing with tip launcher models, demonstrated C_l oscillation main frequencies close to 70 Hz even though significant non-airfoil geometry features were present. Unfortunately, URANS NACA 64A204 airfoil simulations were unable to predict sustained shockwave oscillations using grid and CFD solver settings that produced the best results for OAT15A airfoil simulations. Irregular shockwave effects observed during certain simulations illustrate that the grid and solver requirements for simulating transonic shock-buffet have not been fully quantified. The research results show that unstructured CFD methods can capture shockwave oscillations resulting from SBLI, and highlight how much more work is necessary before computational tools can accurately predict this complex phenomenon on aerospace vehicles.

Acknowledgments

This work was made possible by funding from the Air Force Office of Scientific Research (AFOSR) under Laboratory Task 12RW01COR. The AFOSR program manager was Dr. Michael J. Kendra. The Test Center technology transition advisor was Mr. Jason A. Lechniak. Computational time was provided by the DoD High Performance Computing Modernization Program (HPCMP) under project AFMNG31652E99 entitled, "Fluid-Structure Interaction Analyses of Limit-Cycle Oscillation Flow-Field Physics".

References

[1]Dolling, D. S., "Fifty years of shock-wave/boundary-layer interaction research: what next?" *AIAA Journal*, Vol. 39, No. 8, 2001, pp. 1517–1531.

[2]Raveh, D. and Dowell, E., "Aeroelastic response of an airfoil in buffeting transonic flows," *IFASD Paper 2009-161, International Forum on Aeroelasticity and Structural Dynamics, Seattle, WA*, 2009.

[3]McDevitt, J. and Okuno, A., "Static and dynamic pressure measurements on a NACA 0012 airfoil in the Ames High Reynolds Number Facility. NASA TP-2485," *National Aeronautics and Space Administration*, 1985.

[4]Benoit, B. and Legrain, I., "Buffeting prediction for transport aircraft applications based on unsteady pressure measurements," *AIAA Paper 87-2356, 5th Applied Aerodynamics Conference*, 1987, pp. 225–235.

[5]Jacquin, L., Molton, P., Deck, S., Maury, B., and Soulevant, D., "Experimental study of shock oscillation over a transonic supercritical profile," *AIAA Journal*, Vol. 47, No. 9, 2009, pp. 1985–1994.

[6]Deck, S., "Numerical simulation of transonic buffet over a supercritical airfoil," *AIAA Journal*, Vol. 43, No. 7, 2005, pp. 1556–1566.

[7]Xiao, Q., Tsai, H.-M., and Liu, F., "Numerical study of transonic buffet on a supercritical airfoil," *AIAA journal*, Vol. 44, No. 3, 2006, pp. 620–628.

[8]Crouch, J., Garbaruk, A., Magidov, D., and Travin, A., "Origin of transonic buffet on aerofoils," *Journal of Fluid Mechanics*, Vol. 628, 2009, pp. 357–369.

[9]Thomas, J. P. and Dowell, E. H., "Airfoil Transonic Flow Buffet Calculations Using the OVERFLOW 2 Flow Solver," *AIAA Paper 2011-2007*, 2011.

[10]Iovnovich, M. and Raveh, D. E., "Reynolds-averaged navier–stokes study of the shock-buffet instability mechanism," *AIAA Journal*, Vol. 50, No. 4, 2012, pp. 880–890.

[11]Ren, X., Zhao, Z., Gao, C., Xiong, J., Liu, F., and Luo, S., "Investigation of NACA 0012 airfoil periodic flows in a transonic wind tunnel," *AIAA Paper 2013-791, 50th AIAA Aerospace Sciences Meeting including the New Horizons Forum and Aerospace Exposition*, 2013.

[12]Iovnovich, M. and Raveh, D. E., "Numerical Study of Shock Buffet on Three-Dimensional Wings," *AIAA Journal*, 2014, pp. 1–15.

[13]Zikanov, O., *Essential computational fluid dynamics*, John Wiley & Sons, 2010.

[14]Dowell, E. H., "Transonic unsteady potential flow: Scaling analysis of linear and nonlinear dynamics," *AIAA Journal*, Vol. 48, No. 5, 2010, pp. 1017–1020.

[15]Lechniak, J. A., Bhamidipati, K. K., and Pasiliao, C. L., "Characterizing the aerodynamic influence of F-16 store on limit cycle oscillations using aero-structure simulation," *AIAA Paper 2012-3340, Proceedings of the 28th aerodynamic measurement technology, ground testing, and flight testing conference*, 2012.

[16]Lechniak, J. A. and Bhamidipati, K. K., "Fluid-Structure Interaction Evaluation of F-16 Limit Cycle Oscillations," *AIAA Paper 2012-0042, 50th AIAA Aerospace Sciences Meeting including the New Horizons Forum and Aerospace Exposition*, 2012.

[17]Bhamidipati, K. K., Reasor, D. A., Lechniak, J. A., Pasiliao, C. L., and Kielb, R., "Unsteady reynolds-averaged navier–stokes simulation of shock-buffet instability on the NACA 64A204 using unstructured meshes," *USNCCM12-975, Twelfth US National Congress for Computational Mechanics, Symposium on Advances in Nonlinear Unsteady Aerodynamic Flows, Raleigh, NC, USA*, 2013.

[18]Hartmann, A., Feldhusen, A., and Schröder, W., "On the interaction of shock waves and sound waves in transonic buffet flow," *Physics of Fluids (1994-present)*, Vol. 25, No. 2, 2013, pp. 026101.

[19]Billard, F., *TestCase006OAT15A < ATAAC < TWiki*, 2013 (accessed September 13, 2013), `http://cfd.mace.manchester.ac.uk/twiki/bin/view/ATAAC/TestCase006OAT15A`.

[20]Denegri, C. M., "Limit cycle oscillation flight test results of a fighter with external stores," *Journal of Aircraft*, Vol. 37, No. 5, 2000, pp. 761–769.

[21]Denegri, C. M., Dubben, J. A., and Dawson, K. S., "Underwing missile control-surface effects on aircraft limit cycle oscillations," *Journal of Aircraft*, Vol. 51, No. 2, 2014, pp. 693–695.

[22]Pasiliao, C. L. and Dubben, J. A., "CFD Based Determination of Transonic Flow Field Characteristics of F-16 Wing Associated with LCO," *47th AIAA Aerospace Sciences Meeting including The New Horizons Forum and Aerospace Exposition*, 2009.

[23]Pasiliao, C. L. and Dubben, J. A., "Analysis of CFD Pressure Coefficients on the F-16 Wing Associated with Limit Cycle Oscillations," *AIAA Paper*, Vol. 409, 2008.

[24]Pasiliao, C. L. and Dubben, J. A., "Fluid-Structure Reaction Study of an F-16 Limit Cycle Oscillation Case with Stores," *AIAA 2010*, Vol. 2633.

[25]Biedron, R. T., Derlaga, J. M., Gnoffo, P. A., Hammond, D. P., Jones, W. T., Kelb, B., Lee-Rausch, E. M., Nielsen, E. J., Park, M. A., Rumsey, C. L., Thomas, J. L., and Wood, W. A., "FUN3D Manual: 12.4," Tech. Rep. NASA/TM-2014-218179, Langley Research Center, Hampton, VA, 2014.

[26]Rumsey, C. L., *The Spalart–Allmaras Turbulence Model*, 2013 (accessed September 13, 2013), `http://turbmodels.larc.nasa.gov/spalart.html`.

[27]Rumsey, C. L., *The Menter Shear Stress Transport Turbulence Model*, 2014 (accessed December 5, 2014), `http://turbmodels.larc.nasa.gov/sst.html`.

[28]Oberkampf, W. L. and Roy, C. J., *Verification and Validation in Scientific Computing*, Cambridge University Press, 2010.